Hermite neural network-based second-order sliding-mode control of synchronous reluctance motor drive systems

Yongchao Liu, Salah Laghrouche, Abdoul Diaye, Maurizio Cirrincione

Version of Record: https://www.sciencedirect.com/science/article/pii/S0016003220307341
Manuscript_14c175f2794cccfd81a8c198eabef52b

Hermite neural network-based second-order sliding-mode control of synchronous reluctance motor drive systems

Yong-Chao Liu [a], Salah Laghrouche [a,✉], Abdoul N'Diaye [a], Maurizio Cirrincione [b]

[a] Energy Department, FEMTO-ST Institute (UMR 6174), French National Centre for Scientific Research (CNRS), UTBM, Université Bourgogne Franche-Comté, Belfort, France

[b] School of Engineering and Physics, The University of the South Pacific, Laucala Campus, Suva, Fiji

Email: yongchao.liu@utbm.fr, salah.laghrouche@utbm.fr (✉), abdoul-ousman.n-diaye@utbm.fr, maurizio.cirrincione@usp.ac.fj

Abstract: This paper proposes a novel Hermite neural network-based second-order sliding-mode (HNN-SOSM) control strategy for the synchronous reluctance motor (SynRM) drive system. The proposed HNN-SOSM control strategy is a nonlinear vector control strategy consisting of the speed control loop and the current control loop. The speed control loop adopts a composite speed controller, which is composed of three components: 1) a standard super-twisting algorithm-based SOSM (STA-SOSM) controller for achieving the rotor angular speed tracking control, 2) a HNN-based disturbance estimator (HNN-DE) for compensating the lumped disturbance, which is composed of external disturbances and parametric uncertainties, and 3) an error compensator for compensating the approximation error of the HNN-DE. The learning laws for the HNN-DE and the error compensator are derived by the Lyapunov synthesis approach. In the current control loop, considering the magnetic saturation effect, two composite current controllers, each of which comprises two standard STA-SOSM controllers, are designed to make direct and quadrature axes stator current components in the rotor reference frame track their references, respectively. Comparative hardware-in-the-loop (HIL) tests between the proposed HNN-SOSM control strategy and the conventional STA-SOSM control strategy for the SynRM drive system are performed. The results of the HIL tests validate the feasibility and the superiority of the proposed HNN-SOSM control strategy.

Keywords: Synchronous reluctance motor, second-order sliding-mode control, super-twisting algorithm, Hermite neural network, disturbance estimator.

1 Introduction

In recent years, the synchronous reluctance motor (SynRM) has been regarded as a powerful alternative for the induction motor and the permanent-magnet synchronous motor in the variable-speed drive system due to its magnetless, windingless and cageless rotor structure [1-4]. The SynRM drive system can provide a good compromise between the manufacturing cost and the drive performance. Therefore, it has been successfully applied in some industrial areas, such as the renewable energy conversion system, the electric traction system and the water supply system [5-9].

With respect to the high-performance control of the SynRM drive system, the vector control strategy is one of the most popular choices [7-11]. The existing vector control strategies of the SynRM drive system can be divided into two categories: 1) the dual-loop vector control strategy for the rotor angular speed tracking control, which consist of the speed control loop and the current control loop, and 2) the triple-loop vector control strategy for the rotor position tracking control, which is composed of the position control loop, the speed control loop and the current control loop [12]. The linear proportional-

integral (PI) controller is widely used in the vector-controlled SynRM drive system. However, such a linear controller, which is designed using the linear system model, is sensitive to disturbances and uncertainties [13]. In practice, the SynRM suffers from strong magnetic nonlinearity caused by the magnetic saturation effect, resulting in highly nonlinear relationship between the stator flux linkage and the stator current [14-17]. Furthermore, the drive system is affected by a variety of external disturbances and parametric uncertainties [13]. Therefore, the SynRM drive system is a nonlinear system. In order to accomplish a high-performance vector-controlled SynRM drive system, it is preferred to replace linear PI controllers with well-designed nonlinear controllers in the vector control strategy.

Until now, various nonlinear controllers have been designed for vector control strategies of the SynRM drive system, such as the neural network-based controllers [18, 19], the adaptive controllers [12, 20], the predictive controllers [21, 22], and the sliding-mode controllers (SMCs) [23-27]. Among them, the SMC-based vector control strategies have received considerable attention because of their attractive advantages including robustness and finite-time convergence. In [23], a SMC-based triple-loop vector control strategy has been proposed for the SynRM drive system. In such a vector control strategy, two SMCs are employed by the position and speed control loops, respectively, while two linear PI controllers are adopted by the current control loop. In [24], a combined positon and speed control strategy based on the multi-segment SMC has been proposed for the SynRM drive system. Nevertheless, aforementioned SMCs are dependent on the first-order sliding-mode (FOSM) algorithm, which suffers from severe chattering phenomenon. This phenomenon reduces the control accuracy and increases the losses as well as the noise of the drive system [28-30].

To alleviate the chattering phenomenon in the SMC, several schemes have been proposed [29-32]. Amongst them, the second-order sliding-mode (SOSM) algorithms, which ensure the finite-time convergence of the sliding variable and its time derivative to the origin, have gained much attention [26, 27, 30-45]. The super-twisting algorithm (STA) is an absolutely continuous SMSO algorithm that retains main attractive features of the FOSM algorithm without requiring the information of the time derivative of the sliding variable [30-32]. In recent years, the standard STA-based SOSM (STA-SOSM) controllers and observers have been found wide applications [27, 35-44]. Regarding the SynRM drive system, a STA-SOSM control strategy, which is a dual-loop vector control strategy using a standard STA-SOSM speed controller and two linear PI current controllers, has been proposed in [27]. To design the standard STA-SOSM speed controller, the speed tracking error dynamics is used. In such a dynamics, the lumped disturbance is mainly composed of the mechanical and electrical parametric uncertainties, the lord torque, and the friction torque. In many applications, the load changes frequently from one operating condition to another, often resulting in the sudden and significant change of the lumped disturbance in the speed tracking error dynamics. The standard STA-SOSM speed controller uses the sign function-based nonlinear feedback regulation mechanism to deal with such a strong disturbance. Since the sign function is bounded, theoretically, quite large gains are required by the standard STA-SOSM speed controller to achieve satisfactory tracking performance in the presence of a strong lumped disturbance. However, it aggravates the chattering phenomenon in practice. A solution to such an issue is the development of a composite speed controller which combines the standard STA-SOSM controller with a high-performance disturbance estimator (DE). In this speed controller, the DE is used to compensate the lumped disturbance

in the speed tracking error dynamics in real time, such that relatively small gains are enough for the standard STA-SOSM controller adopted by the composite speed controller to achieve satisfactory tracking performance. With respect to the design of two stator current controllers, two current tracking error dynamics in the rotor reference frame are adopted. In these two dynamics, the lumped disturbances mainly consist of the electrical parametric uncertainties and the disturbance voltages caused by the effects of the inverter nonlinearities. Usually, such disturbance voltages do not change suddenly and significantly [46-49]. The magnetic saturation effect is one of the main causes of above-mentioned electrical parametric uncertainties. Such an effect make each current tracking error dynamics in the rotor reference frame become a nonlinear system in terms of both direct and quadrature axes stator current components [14-17]. It means that the use of two linear PI current controllers cannot address the robust stator current tracking control problem. Therefore, two robust nonlinear current controllers should be developed for the vector control strategy of the SynRM drive system.

It is widely recognized that well-designed single hidden layer feedforward neural networks (SHLFNNs) can serve as high-performance DEs for control applications due to their good approximation abilities [50]. In [51], a composite controller, which combines a standard STA-SOSM controller with a radial basis function neural network-based DE (RBFNN-DE), has been proposed for the micro-gyroscope. However, the presented stability analysis for the tracking error dynamics using this composite controller is *not rigorous*. Furthermore, the values of the center and the width of each Gaussian basis function in the hidden layer of the RBFNN-DE are chosen offline by means of simulation-based trial-and-error approach. Regarding the lumped disturbance in the speed tracking error dynamics of the SynRM drive system, it can be described as a combination of a constant term, a linear term, second-order nonlinear terms and high-order nonlinear terms in the sense of the series expansion. As long as a sufficient number of terms in a series are adopted, the weighted sum of them can approximate any function to any degree of accuracy [54]. Due to this attractive feature, several orthogonal polynomial basis functions, such as Chebyshev polynomial basis functions, Legendre polynomial basis functions and Hermite polynomial basis functions, have been selected as activation functions in the hidden layer to construct different SHLFNNs [52-60]. Among them, the Hermite polynomial basis function-based SHLFNN, or as often called the Hermite neural network (HNN), has a more efficient search space and better representational ability due to the unlimited input range of the Hermite polynomial basis functions [57]. Moreover, there is no need for each activation function in the hidden layer of the HNN to choose any parameter offline. Because of these attractive features, the HNN has been used to design the DE for improving the tracking performance of the SMC. In [60], a composite controller, which consists of a nonsingular terminal SMC, a HNN-based DE (HNN-DE) and an error compensator, has been proposed for the nonlinear magnetic bearing system. However, in order to obtain the nonsigular terminal sliding variable and the learning laws for this HNN-DE, a quite complex fractional exponent term with respect to the time derivative of the tracking error has to be calculated online, which increases the implementation complexity of such a composite controller.

In this paper, considering external disturbances and parametric uncertainties of the SynRM drive system, a novel HNN-based SOSM (HNN-SOSM) control strategy is proposed for the SynRM drive system. The proposed control strategy is a dual-loop vector control strategy. The main contributions can be summarized as follows.

1) In the speed control loop, a composite speed controller consisting of a standard STA-SOSM controller, a HNN-DE and an error compensator is proposed to regulate the rotor angular speed. Rigorous stability analysis for the speed tracking error dynamics using such a controller is presented. Based on that, the learning laws for the HNN-DE and the error compensator are derived.
2) In the current control loop, two composite current controllers, each of which consists of two standard STA-SOSM controllers, are proposed to regulate direct and quadrature axes stator current components in the rotor reference frame. Rigorous stability analyses for two current tracking error dynamics using such controllers are presented.
3) The performance of the proposed HNN-SOSM control strategy is compared with that of the conventional STA-SOSM control strategy based on a standard STA-SOSM speed controller and two linear PI current controllers.

The rest of this paper is organized as follows. In Section 2, the mathematical model of the two-level voltage-source inverter (2L-VSI)-fed SynRM drive system is presented. In Section 3, the design of the adopted HNN-DE is presented. In Section 4, the design and the rigorous stability analysis of the composite controller, which consists of a standard STA-SOSM controller, a HNN-DE and an error compensator, are presented. In Section 5, the proposed HNN-SOSM control strategy is described in detail. In Section 6, the results of the comparative hardware-in-the-loop (HIL) tests between the proposed HNN-SOSM control strategy and the conventional STA-SOSM control strategy are presented and analyzed. The conclusions are given in Section 7.

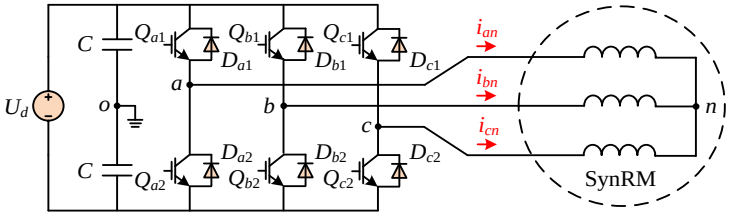

Fig. 1. The 2L-VSI-fed SynRM drive system.

2 Problem formulation

2.1 Mathematical model of the 2L-VSI

The 2L-VSI-fed SynRM drive system is illustrated in Fig.1, where U_d is the dc-bus voltage, C is the dc-bus capacitor, Q_{a1}-Q_{c2} are six power switching devices, D_{a1}-D_{c2} are six freewheeling diodes, i_{an}, i_{bn} and i_{cn} are three-phase stator currents. With respect to the mathematical model of the 2L-VSI, the effects of the inverter nonlinearities including the dead time, the turn-on/off time, the saturation voltage of the power switching device and the diode forward voltage are taken into account. At first, the switching function for each leg of the 2L-VSI is defined as

$$S_x = \begin{cases} 1, & \text{if } Q_{x1} \text{ on}, Q_{x2} \text{ off} \\ 0, & \text{if } Q_{x1} \text{ off}, Q_{x2} \text{ on} \end{cases}, \quad x = a, b, c \tag{1}$$

Regarding each phase of the 2L-VSI, within a switching period T_s, the relationship between the actual and applied conducting time of the upper power switching device Q_{x1} can be expressed as (2), and the corresponding high-frequency model of the pole voltage can be described as (3) [46-49].

$$T_x = T_x^* + \left(T_{off} - T_{on} - T_{dead}\right)\mathrm{sgn}\left(i_{xn}\right) \tag{2}$$

$$u_{xo} = (U_{dc} - U_{sat} + U_{diode})\left(S_x - \frac{1}{2}\right) - \frac{1}{2}(U_{sat} + U_{diode})\mathrm{sgn}(i_{xn}) \tag{3}$$

where T_x and T_x^* denote the actual and applied conducting time of Q_{x1}, respectively, T_{on}, T_{off}, T_{dead} represent the turn-on time, the turn-off time and the dead time of the power switching device, respectively, U_{sat} and U_{diode} denote the saturation voltage of the power switching device and the diode forward voltage of the freewheeling diode, respectively, u_{xo} is the pole voltage for the phase x, and sgn(•) is the sign function written as

$$\mathrm{sgn}(i_{xn}) = \begin{cases} +1, & \text{if } i_{xn} > 0 \\ 0, & \text{if } i_{xn} = 0 \\ -1, & \text{if } i_{xn} < 0 \end{cases} \tag{4}$$

Based on (2), the actual duty cycle d_x, which denotes the average value of S_x in a switching period, is expressed as

$$d_x = \frac{T_x}{T_s} = d_x^* + \frac{T_{off} - T_{on} - T_{dead}}{T_s}\mathrm{sgn}(i_{xn}) \tag{5}$$

where $d_x^* = \frac{T_x^*}{T_s}$ denotes the applied duty cycle of Q_{x1}

By replacing S_x in (3) with d_x, the low-frequency model of the pole voltage considering the effects of the inverter nonlinearities can be derived as

$$u_{xo} = (U_{dc} - U_{sat} + U_{diode})\left(d_x^* - \frac{1}{2}\right) + U_{dead}\mathrm{sgn}(i_{xn}) \tag{6}$$

where U_{dead} is written as

$$U_{dead} = (U_{dc} - U_{sat} + U_{diode})\frac{T_{off} - T_{on} - T_{dead}}{T_s} - \frac{U_{sat} + U_{diode}}{2} \tag{7}$$

For the balanced three-phase loads, the three-phase stator voltages u_{an}, u_{bn} and u_{cn} can be calculated as

$$\begin{bmatrix} u_{an} \\ u_{bn} \\ u_{cn} \end{bmatrix} = \frac{1}{3}\begin{bmatrix} 2 & -1 & -1 \\ -1 & 2 & -1 \\ -1 & -1 & 2 \end{bmatrix}\begin{bmatrix} u_{ao} \\ u_{bo} \\ u_{co} \end{bmatrix} \tag{8}$$

Substituting (6) into (8), the low-frequency model of the 2L-VSI considering the effects of the inverter nonlinearities is derived as

$$\begin{cases} u_{an} = \underbrace{\frac{2d_a^* - d_b^* - d_c^*}{3}U_{dc}}_{u_{an}^*} + \underbrace{\frac{2d_a^* - d_b^* - d_c^*}{3}(U_{diode} - U_{sat}) + \frac{U_{dead}}{3}\left[2\mathrm{sgn}(i_{an}) - \mathrm{sgn}(i_{bn}) - \mathrm{sgn}(i_{cn})\right]}_{u_{an}^d} = u_{an}^* + u_{an}^d \\ u_{bn} = \underbrace{\frac{2d_b^* - d_a^* - d_c^*}{3}U_{dc}}_{u_{bn}^*} + \underbrace{\frac{2d_b^* - d_a^* - d_c^*}{3}(U_{diode} - U_{sat}) + \frac{U_{dead}}{3}\left[2\mathrm{sgn}(i_{bn}) - \mathrm{sgn}(i_{an}) - \mathrm{sgn}(i_{cn})\right]}_{u_{bn}^d} = u_{bn}^* + u_{bn}^d \\ u_{cn} = \underbrace{\frac{2d_c^* - d_a^* - d_b^*}{3}U_{dc}}_{u_{cn}^*} + \underbrace{\frac{2d_c^* - d_a^* - d_b^*}{3}(U_{diode} - U_{sat}) + \frac{U_{dead}}{3}\left[2\mathrm{sgn}(i_{cn}) - \mathrm{sgn}(i_{an}) - \mathrm{sgn}(i_{bn})\right]}_{u_{cn}^d} = u_{cn}^* + u_{cn}^d \end{cases} \tag{9}$$

where u_{an}^*, u_{bn}^* and u_{cn}^* represent ideal three-phase stator voltages, u_{an}^d, u_{bn}^d and u_{cn}^d denote the three-phase disturbance voltages caused by the effects of the inverter nonlinearities.

2.2 Mathematical model of the SynRM

With respect to the SynRM, considering the effects of the magnetic saturation and the inverter nonlinearities, its stator voltage and stator flux linkage equations in the rotor reference frame can be expressed as (10) and (11), respectively.

$$u_{sd} = u_{sd}^{*} + u_{sd}^{d} = R_s i_{sd} + \frac{d\lambda_{sd}}{dt} - n_p \omega_m \lambda_{sq}, \quad u_{sq} = u_{sq}^{*} + u_{sq}^{d} = R_s i_{sq} + \frac{d\lambda_{sq}}{dt} + n_p \omega_m \lambda_{sd} \tag{10}$$

$$\lambda_{sd} = \lambda_{sd}\left(i_{sd}, i_{sq}\right) = L_d\left(i_{sd}, i_{sq}\right) i_{sd}, \quad \lambda_{sq} = \lambda_{sq}\left(i_{sd}, i_{sq}\right) = L_q\left(i_{sd}, i_{sq}\right) i_{sq} \tag{11}$$

where u_{sd} and u_{sq} are the direct and quadrature axes stator voltage components, respectively, u_{sd}^{*} and u_{sq}^{*} are the ideal direct and quadrature axes stator voltage components, respectively, u_{sd}^{d} and u_{sq}^{d} are the direct and quadrature axes disturbance voltage components caused by the effects of the inverter nonlinearities, respectively, i_{sd} and i_{sq} are the direct and quadrature axes stator current components, respectively, L_d and L_q are the apparent inductances, λ_{sd} and λ_{sq} are the direct and quadrature axes stator flux linkage components, respectively, R_s represents the stator resistance, n_p is the pole pairs, and ω_m denotes the rotor mechanical angular speed.

Since both λ_{sd} and λ_{sq} are nonlinear functions in terms of i_{sd} and i_{sq}, the following equations can be obtained [61].

$$\frac{d\lambda_{sd}}{dt} = L_{dd}\frac{di_{sd}}{dt} + L_{dq}\frac{di_{sq}}{dt}, \quad \frac{d\lambda_{sq}}{dt} = L_{qd}\frac{di_{sd}}{dt} + L_{qq}\frac{di_{sq}}{dt} \tag{12}$$

where L_{dd}, L_{dq}, L_{qd}, and L_{qq} are the incremental inductances calculated as follow [61]:

$$\begin{aligned} L_{dd} &= \frac{\partial\lambda_{sd}}{\partial i_{sd}} \approx \left.\frac{\Delta\lambda_{sd}}{\Delta i_{sd}}\right|_{i_{sq}=\text{constant}}, \quad L_{dq} = \frac{\partial\lambda_{sd}}{\partial i_{sq}} \approx \left.\frac{\Delta\lambda_{sd}}{\Delta i_{sq}}\right|_{i_{sd}=\text{constant}} \\ L_{qd} &= \frac{\partial\lambda_{sq}}{\partial i_{sd}} \approx \left.\frac{\Delta\lambda_{sq}}{\Delta i_{sd}}\right|_{i_{sq}=\text{constant}}, \quad L_{qq} = \frac{\partial\lambda_{sq}}{\partial i_{sq}} \approx \left.\frac{\Delta\lambda_{sq}}{\Delta i_{sq}}\right|_{i_{sd}=\text{constant}} \end{aligned} \tag{13}$$

The reluctance torque equation of the SynRM is described as follow [1]:

$$T_r = \frac{3}{2} n_p \left(\lambda_{sd} i_{sq} - \lambda_{sq} i_{sd}\right) \tag{14}$$

where T_r is the reluctance torque.

In this paper, the viscous friction torque, which is dependent on the rotor angular speed, is considered as the main contributor to the friction torque of the SynRM. Thus, the friction torque equation of the SynRM can be described as follow [62]:

$$T_f = B_m \omega_m \tag{15}$$

where T_f is the friction torque, B_m denotes the viscous friction coefficient.

The motion equation of the SynRM is expressed as follow [62]:

$$J\frac{d\omega_m}{dt} = T_r - T_l - T_f \tag{16}$$

where J is the rotor inertia and T_l denotes the load torque.

Based on (10)-(16), the dynamic model of the SynRM in terms of i_{sd}, i_{sq} and ω_m can be derived as

$$\begin{cases} \dfrac{di_{sd}}{dt} = \dfrac{L_{qq}}{M}\left(u_{sd}^{*} + u_{sd}^{d} - R_s i_{sd} + n_p \omega_m L_q i_{sq}\right) - \dfrac{L_{dq}}{M}\left(u_{sq}^{*} + u_{sq}^{d} - R_s i_{sq} - n_p \omega_m L_d i_{sd}\right) \\ \dfrac{di_{sq}}{dt} = -\dfrac{L_{qd}}{M}\left(u_{sd}^{*} + u_{sd}^{d} - R_s i_{sd} + n_p \omega_m L_q i_{sq}\right) + \dfrac{L_{dd}}{M}\left(u_{sq}^{*} + u_{sq}^{d} - R_s i_{sq} - n_p \omega_m L_d i_{sd}\right) \\ \dfrac{d\omega_m}{dt} = \dfrac{3n_p}{2J}\left(L_d - L_q\right) i_{sd} i_{sq} - \dfrac{1}{J} T_l - \dfrac{1}{J} T_f \end{cases} \tag{17}$$

where $M = L_{dd}L_{qq} - L_{dq}L_{qd}$.

2.3 External disturbances and parametric uncertainties

From (17), it can be seen that the dynamic model of the SynRM contains u_{sd}^{d}, u_{sq}^{d}, T_l, T_f, and parameters including L_d, L_q, L_{dd}, L_{dq}, L_{qd}, L_{qq}, R_s and J. In practice, their values are not constant and usually vary with different operating conditions of the SynRM drive system. In this paper, u_{sd}^{d}, u_{sq}^{d}, T_l and T_f are regarded as the external disturbances. As for the parametric uncertainties, the variations of L_d, L_q, L_{dd}, L_{dq}, L_{qd}, L_{qq}, R_s and J are considered.

Up to now, several models have been proposed to formulate apparent inductances based on measured data [14-17]. In this paper, the apparent inductance model proposed in [14], which can approximate the values of L_d and L_q for different combinations of i_{sd} and i_{sq} in a wide range, is adopted. According to such a model, L_d and L_q can be formulated as

$$L_d\left(i_{sd}, i_{sq}\right) = L_{d0}\left(i_{sd}\right) - L_{d1}\left(i_{sd}\right) L_{q2}\left(i_{sq}\right), \quad L_q\left(i_{sd}, i_{sq}\right) = L_{q0}\left(i_{sq}\right) - L_{d2}\left(i_{sd}\right) L_{q1}\left(i_{sq}\right) \tag{18}$$

where

$$L_{d0}\left(i_{sd}\right) = c_{d0} + c_{d1} \Big/ \left(i_{sd}^4 + c_{d2} i_{sd}^2 + c_{d3}\right), \quad L_{d1}\left(i_{sd}\right) = c_{d4} \Big/ \left(i_{sd}^4 + c_{d5} i_{sd}^2 + c_{d6}\right), \quad L_{d2}\left(i_{sd}\right) = 1 - 1 \Big/ \left(c_{dq} i_{sd}^2 + 1\right)$$
$$L_{q0}\left(i_{sq}\right) = c_{q0} + c_{q1} \Big/ \left(i_{sq}^4 + c_{q2} i_{sq}^2 + c_{q3}\right), \quad L_{q1}\left(i_{sq}\right) = c_{q4} \Big/ \left(i_{sq}^4 + c_{q5} i_{sq}^2 + c_{q6}\right), \quad L_{q2}\left(i_{sq}\right) = 1 - 1 \Big/ \left(c_{qd} i_{sq}^2 + 1\right)$$

Based on (11), (13) and (18), the incremental inductances can also be formulated. Defining L_{d0}, L_{q0}, L_{dd0}, L_{dq0}, L_{qd0}, and L_{qq0} as nominal apparent and incremental inductances for a certain combination of i_{sd} and i_{sq}, the apparent and incremental inductances can be expressed as

$$\begin{aligned} &L_d\left(i_{sd}, i_{sq}\right) = L_{d0} + \Delta L_d, \quad L_q\left(i_{sd}, i_{sq}\right) = L_{q0} + \Delta L_q \\ &L_{dd}\left(i_{sd}, i_{sq}\right) = L_{dd0} + \Delta L_{dd}, \quad L_{dq}\left(i_{sd}, i_{sq}\right) = L_{dq0} + \Delta L_{dq} \\ &L_{qd}\left(i_{sd}, i_{sq}\right) = L_{qd0} + \Delta L_{qd}, \quad L_{qq}\left(i_{sd}, i_{sq}\right) = L_{qq0} + \Delta L_{qq} \end{aligned} \tag{19}$$

where ΔL_d, ΔL_q, ΔL_{dd}, ΔL_{dq}, ΔL_{qd}, and ΔL_{qq} are parametric uncertainties in respect of L_d, L_q, L_{dd}, L_{dq}, L_{qd}, and L_{qq}, respectively, for different combinations of i_{sd} and i_{sq}.

With regard to R_s and J, they can be rewritten as

$$R_s = R_{s0} + \Delta R_s, \quad J = J_0 + \Delta J \tag{20}$$

where R_{s0} and J_0 are nominal values of R_s and J, respectively, ΔR_s and ΔJ denote parametric uncertainties in respect of R_s and J, respectively.

2.4 Control objectives

The control objectives of the dual-loop vector control strategy of the SynRM drive system can be summarized as follow:

1) ω_m should track its reference ω_{mr}.
2) i_{sd} and i_{sq} should track their references i_{sdr} and i_{sqr}, respectively.

3 Disturbance estimator design

In this section, the Hermite functions are introduced. Based on them, a single-input-single-output HNN-DE is designed.

3.1 Hermite functions

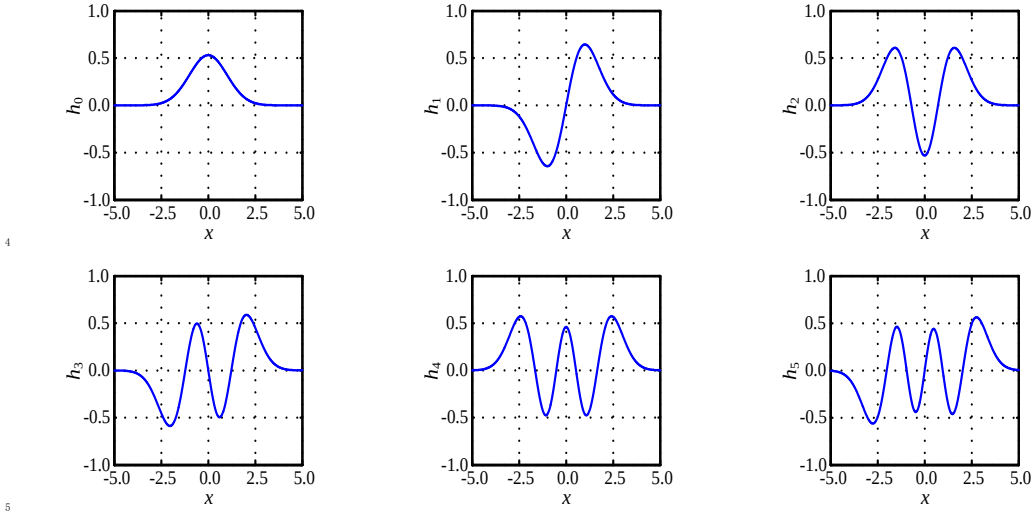

Fig. 2 First six Hermite functions.

The Hermite polynomials $\{H_n(x)\}_{n=0}^{\infty}$, which is defined in the interval $(-\infty, \infty)$, can be expressed by the following so-called Rodrigues' formula [54].

$$H_n(x)=(-1)^n e^{x^2}\frac{d^n}{dx^n}\left(e^{-x^2}\right), \quad n=0,1,2,... \tag{21}$$

Based on (21), a useful recurrence relation to calculate each $H_n(x)$ can be derived as

$$H_0(x)=1, \quad H_1(x)=2x, \quad H_n(x)=2xH_{n-1}(x)-2(n-1)H_{n-2}(x), \quad n>2 \tag{22}$$

Although $\{H_n(x)\}_{n=0}^{\infty}$ are orthogonal with regard to the weight function $\kappa(x)=e^{-x^2}$, they are not orthonormal. Regarding polynomial-based activation functions in the hidden layer of the SHLFNN, the orthonormal polynomials are preferred [56-60]. Toward this end, based on $\{H_n(x)\}_{n=0}^{\infty}$, the so-called Hermite functions $\{h_n(x)\}_{n=0}^{\infty}$, which are orthonormal functions, are derived as follow [56-60]:

$$h_n(x)=\frac{1}{\sqrt{\sqrt{\pi}2^n n!}}H_n(x)e^{-x^2/2} \tag{23}$$

The first six Hermite functions are illustrated in Fig. 2.

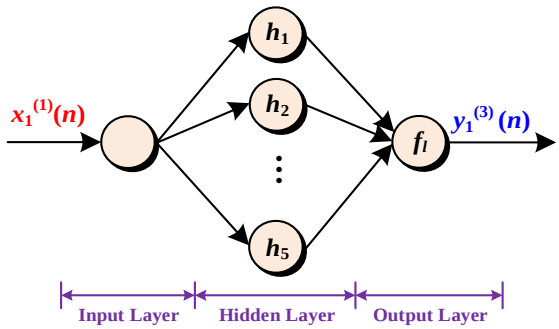

Fig. 3 The block diagram of the HNN-DE.

3.2 HNN-DE

The structure of the HNN-DE adopted in this paper is illustrated in Fig. 3. Such a DE consists of the input layer, the hidden layer and the output layer. The first five Hermite functions are selected as the activation functions in the hidden layer, while the linear function is selected as the activation function in the output layer. The signal propagation in each layer of the HNN-DE is introduced as follows.

There is one node in the input layer. The signal propagation of such a node is described as

$$y_1^{(1)}(n) = x_1^{(1)}(n) \tag{24}$$

where n represents the nth iteration, $x_1^{(1)}(n)$ and $y_1^{(1)}(n)$ are the input and output signals of the node in the input layer, respectively.

There are five nodes in the hidden layer. For the ith node ($i = 1, 2, 3, 4, 5$), the signal propagation is described as

$$x_i^{(2)}(n) = y_1^{(1)}(n) \tag{25}$$

$$y_i^{(2)}(n) = h_i\left(x_i^{(2)}(n)\right) \tag{26}$$

where $x_i^{(2)}(n)$ and $y_i^{(2)}(n)$ are the input and output signals of the ith node in the hidden layer, respectively, and $h_i(\cdot)$ is the ith Hermite function.

There is one node in the output layer. The signal propagation of such a node is described as

$$x_1^{(3)}(n) = \sum_{i=1}^{5} W_i(n)\, y_i^{(2)}(n) \tag{27}$$

$$y_1^{(3)}(n) = f_l\left(x_1^{(3)}(n)\right) = x_1^{(3)}(n) \tag{28}$$

where $x_1^{(3)}(n)$ and $y_1^{(3)}(n)$ are the input and output signals of the node in the output layer, respectively, $W_i(n)$ denotes the ith output weight, and $f_l(\cdot)$ represents the linear activation function.

Remark 1 In the HNN-DE, all elements in the output weight vector $\boldsymbol{W} = [W_1, W_2, W_3, W_4, W_5]^T$ need to be updated online. To maintain the stability of the control system, the learning laws for the update of $\boldsymbol{W}$ should be derived by the Lyapunov synthesis approach [60].

4 Controller design

In this section, the design of the standard STA-SOSM controller for a single-input uncertain nonlinear system is briefly introduced. Afterward, a composite controller composed of a standard STA-SOSM controller, a HNN-DE and an error compensator is developed. The rigorous stability analysis for the dynamics of the sliding variable using the proposed composite controller is presented. Based on that, the learning laws for the HNN-DE and the error compensator are derived.

4.1 Design of the standard STA-SOSM controller

Considering a single-input uncertain nonlinear system represented by the following form [33].

$$\frac{dx}{dt} = a(x,t) + b(x,t)\mu, \quad e_s = e_s(x,t) \tag{29}$$

where $x \in R^n$ is the state vector, $\mu \in R$ denotes the control law, $e_s(x,t)$: $R^{n+1} \rightarrow R$ is the sliding variable and the only measured output signal, $a(x,t)$ and $b(x,t)$ are smooth uncertain functions.

The control objective is to let e_s and its time derivative converge to the origin in a finite time, and keep it at the origin thereafter. Assuming that the input-output dynamics of the system (29) is a relative

degree one system and the internal dynamics are stable, the input-output dynamics of the system (29) can be described as

$$\frac{d}{dt}e_s(x,t)=\frac{\partial e_s}{\partial t}+\frac{\partial e_s}{\partial x}\left(a(x,t)+b(x,t)\mu\right)=\underbrace{\frac{\partial e_s}{\partial t}+\frac{\partial e_s}{\partial x}a(x,t)}_{\varphi(x,t)}+\underbrace{\frac{\partial e_s}{\partial x}b(x,t)}_{g(x,t)}\mu=\varphi(x,t)+g(x,t)\mu \tag{30}$$

where $\varphi(x,t)$ and $g(x,t)$ are smooth uncertain functions.

Assuming that $g(x,t)$ can be described as

$$g(x,t)=g_0(x,t)+\Delta g(x,t) \tag{31}$$

where $g_0(x,t) > 0$ is a known function and $\Delta g(x,t)$ is the bounded uncertainty for $\forall x \in R^n$ and $t \in [0, \infty)$.

Substituting (31) into (30), the input-output dynamics of the system (29) can be rewritten as

$$\frac{de_s}{dt}=\varphi(x,t)+\left(\Delta g(x,t)+g_0(x,t)\right)\mu \tag{32}$$

Regarding the system (32), the standard STA-SOSM control law μ_s can be designed as follow [30-32]:

$$\mu_s=\frac{1}{g_0(x,t)}\left(-p_1\sqrt{|e_s|}\,\mathrm{sgn}(e_s)-p_2\int\mathrm{sgn}(e_s)dt\right) \tag{33}$$

where p_1 and p_2 are positive constant gains.

Substituting (33) into (32), the dynamics of e_s using the standard STA-SOSM control law can be written as

$$\begin{aligned}\frac{de_s}{dt}&=\varphi(x,t)+\left(g_0(x,t)+\Delta g(x,t)\right)\mu_s=\underbrace{\varphi(x,t)+\Delta g(x,t)\mu_s}_{\gamma_1(x,t)}+g_0(x,t)\mu_s\\&=-p_1\sqrt{|e_s|}\,\mathrm{sgn}(e_s)-p_2\int\mathrm{sgn}(e_s)dt+\gamma_1(x,t)\end{aligned} \tag{34}$$

where $\gamma_1(x,t)$ is the lumped disturbance.

Assuming that $\gamma_1(x,t)$ is differentiable, the system (34) can be converted to the following system.

$$\frac{de_s}{dt}=-p_1\sqrt{|e_s|}\,\mathrm{sgn}(e_s)+\phi_1,\quad \frac{d\phi_1}{dt}=-p_2\mathrm{sgn}(e_s)+\rho_1(x,t) \tag{35}$$

where $\rho_1(x,t)$ is the time derivative of $\gamma_1(x,t)$.

Definition 1 [63, 64]. The system is said to be globally finite-time stable if it is globally asymptotically stable in the sense of Lyapunov with a finite settling time for any solution and initial conditions.

The following Theorem can be used to select p_1 and p_2 for the standard STA-SOSM control law to ensure the globally finite-time stability of the system (35).

Theorem 1 [44, 45] *Considering the system* (35), *suppose* ρ_1 *is bounded as* (36) *for a positive constant* δ_1 *and the Lyapunov candidate function* V_s *designed as* (37) *is used to perform the stability analysis. Then, if* p_1 *and* p_2 *are selected as* (38), *the origin is a globally finite-time-stable equilibrium point. Moreover, the corresponding settling-time function* T_1 *for the finite-time convergence of all trajectories of the system* (35) *to the origin is upper bounded by* (39).

$$|\rho_1|\le\delta_1 \tag{36}$$

$$V_s=\xi^T P\xi \tag{37}$$

$$p_1 > 8, \quad p_2 > \frac{4p_1 + \delta_1}{4(p_1 - 8)} \tag{38}$$

$$T_1 \le \frac{2\sqrt{V_s(\xi_0)}}{q_1} \tag{39}$$

where $\xi = [\sqrt{|e_s|}\mathrm{sgn}(e_s), \phi_1]^T$, ξ_0 is the initial condition of ξ, q_1 is a constant related to p_1, p_2 and ρ_1, P is a positive definite matrix expressed as

$$P = \begin{bmatrix} 4p_2 + p_1^2 & -p_1 \\ -p_1 & 2 \end{bmatrix}$$

4.2 Design of the proposed composite controller

From (34), it can be seen that the standard STA-SOSM control law uses the sign function-based feedback regulation mechanism to guarantee the finite-time convergence of e_s to the origin and reject the lumped disturbance. In general, the selection of p_1 and p_2 has to trade off the disturbance rejection and the chattering phenomenon. Moreover, as mentioned in Section 1, quite large values of p_1 and p_2 need to be selected for achieving satisfactory control performance in the presence of a strong lumped disturbance. Nevertheless, it aggravates the chattering phenomenon. To tackle such a limitation, a composite controller combining the standard STA-SOSM control law with the HNN-DE and the error compensator is developed in this subsection. In this composite controller, the sign function-based feedback regulation mechanism mainly focus on guaranteeing the finite-time convergence of e_s to the origin, and the disturbance rejection is mainly accomplished by the HNN-DE-based feedforward compensation mechanism. Therefore, the selection of p_1 and p_2 can mainly focus on the control performance specifications. It means that, with the same values of p_1 and p_2, the composite controller can achieve better control performance than the standard STA-SOSM controller in the presence of a strong lumped disturbance. Regarding the error compensator, it is used to compensate the approximation error of the HNN-DE.

The proposed composite control law μ_c is designed as

$$\mu_c = \mu_s - y_h - y_c \tag{40}$$

$$y_h = \frac{\boldsymbol{W}^T \boldsymbol{y}^{(2)}}{g_0(x,t)} \tag{41}$$

$$y_c = \frac{\varepsilon_h}{g_0(x,t)} \tag{42}$$

where y_h and y_c denote the HNN-DE term and the error compensation term in the composite control law, respectively, and ε_h is the estimated minimum approximation error for the HNN-DE.

Substituting (40) into (32), the dynamics of e_s using the proposed composite control law can be expressed as

$$\begin{aligned} \frac{de_s}{dt} &= \varphi(x,t) + \left(g_0(x,t) + \Delta g(x,t)\right)\mu_c = \underbrace{\varphi(x,t) + \Delta g(x,t)\mu_c}_{\gamma_2(x,t)} + g_0(x,t)\mu_c \\ &= -p_1\sqrt{|e_s|}\mathrm{sgn}(e_s) - p_2\int \mathrm{sgn}(e_s)dt - \boldsymbol{W}^T\boldsymbol{y}^{(2)} - \varepsilon_h + \gamma_2(x,t) \end{aligned} \tag{43}$$

where $\gamma_2(x,t)$ is the lumped disturbance.

Regarding the HNN-DE adopted by the proposed composite controller, e_s is selected as the input signal, i.e., $x_1^{(1)} = e_s$. Based on the universal approximation property, there is an optimal output weight vector $\boldsymbol{W}^* = [W_1^*,\ W_2^*,\ W_3^*,\ W_4^*,\ W_5^*]^T$ for the HNN-DE, such that the lumped disturbance in (43) can be expressed as

$$\gamma_2 = \boldsymbol{W}^{*T}\boldsymbol{y}^{(2)} + \varepsilon_h^* \tag{44}$$

where $\boldsymbol{y}^{(2)} = [y_1^{(2)},\ y_2^{(2)},\ y_3^{(2)},\ y_4^{(2)},\ y_5^{(2)}]^T$ is the output signal vector of the hidden layer of the HNN-DE, ε_h^* is the minimum approximation error of the HNN-DE.

Assumption 1 All elements in $\boldsymbol{W}^*$ and ε_h^* can be considered as constants in each sampling period.

Substituting (44) into (43), the dynamics of e_s using the proposed composite control law can be rewritten as

$$\begin{aligned}\frac{de_s}{dt} &= -p_1\sqrt{|e_s|}\,\mathrm{sgn}(e_s) - p_2\int \mathrm{sgn}(e_s)\,dt - \boldsymbol{W}^T\boldsymbol{y}^{(2)} - \varepsilon_h + \boldsymbol{W}^{*T}\boldsymbol{y}^{(2)} + \varepsilon_h^* \\ &= -p_1\sqrt{|e_s|}\,\mathrm{sgn}(e_s) - p_2\int \mathrm{sgn}(e_s)\,dt - \Delta\boldsymbol{W}^T\boldsymbol{y}^{(2)} - \Delta\varepsilon_h\end{aligned} \tag{45}$$

where $\Delta\boldsymbol{W} = \boldsymbol{W} - \boldsymbol{W}^* = [\Delta W_1, \Delta W_2, \Delta W_3, \Delta W_4, \Delta W_5]^T$, and $\Delta\varepsilon = \varepsilon_h - \varepsilon_h^*$.

The following Theorem can be used to rigorously derive the learning laws for the HNN-DE and the error compensator adopted by the proposed composite controller.

Theorem 2 *Considering the system* (45) *and the composite control law* (40), *if* p_1 *and* p_2 *are positive constants and the learning laws for the HNN-DE and the error compensator are designed as* (46) *and* (47), *respectively, the origin is a globally asymptotically stable equilibrium point*.

$$\frac{d\boldsymbol{W}}{dt} = \eta_1 p_2 \mathrm{sgn}(e_s)\,\boldsymbol{y}^{(2)} \tag{46}$$

$$\frac{d\varepsilon_h}{dt} = \eta_2 p_2 \mathrm{sgn}(e_s) \tag{47}$$

where η_1 and η_2 are positive learning rates.

Proof At first, the system (45) is converted to the following equivalent system.

$$\frac{de_s}{dt} = -p_1\sqrt{|e_s|}\,\mathrm{sgn}(e_s) + \phi_2 - \Delta\boldsymbol{W}^T\boldsymbol{y}^{(2)} - \Delta\varepsilon_h, \quad \frac{d\phi_2}{dt} = -p_2\mathrm{sgn}(e_s) \tag{48}$$

With regard to the system (48), the following Lyapunov candidate function V_{c1} is chosen.

$$V_{c1} = p_2|e_s| + \frac{1}{2}\phi_2^2 + \frac{1}{2\eta_1}\Delta\boldsymbol{W}^T\Delta\boldsymbol{W} + \frac{1}{2\eta_2}\Delta\varepsilon_h^2 \tag{49}$$

Considering the Assumption 1, the time derivative of V_{c1} can be calculated as

$$\frac{dV_{c1}}{dt} = p_2\mathrm{sgn}(e_s)\frac{de_s}{dt} + \phi_2\frac{d\phi_2}{dt} + \frac{1}{\eta_1}\Delta\boldsymbol{W}^T\frac{d\boldsymbol{W}}{dt} + \frac{1}{\eta_2}\Delta\varepsilon_h\frac{d\varepsilon_h}{dt} \tag{50}$$

Substituting (48) into (50), the following equation can be obtained.

$$\begin{aligned}\frac{dV_{c1}}{dt} &= p_2\mathrm{sgn}(e_s)\left(-p_1\sqrt{|e_s|}\,\mathrm{sgn}(e_s) + \phi_2 - \Delta\boldsymbol{W}^T\boldsymbol{y}^{(2)} - \Delta\varepsilon_h\right) - \phi_2 p_2\mathrm{sgn}(e_s) + \frac{1}{\eta_1}\Delta\boldsymbol{W}^T\frac{d\boldsymbol{W}}{dt} + \frac{1}{\eta_2}\Delta\varepsilon_h\frac{d\varepsilon_h}{dt} \\ &= -p_1p_2\sqrt{|e_s|} - p_2\mathrm{sgn}(e_s)\Delta\boldsymbol{W}^T\boldsymbol{y}^{(2)} - p_2\mathrm{sgn}(e_s)\Delta\varepsilon_h + \frac{1}{\eta_1}\Delta\boldsymbol{W}^T\frac{d\boldsymbol{W}}{dt} + \frac{1}{\eta_2}\Delta\varepsilon_h\frac{d\varepsilon_h}{dt} \\ &= -p_1p_2\sqrt{|e_s|} + \Delta\boldsymbol{W}^T\left(\frac{1}{\eta_1}\frac{d\boldsymbol{W}}{dt} - p_2\mathrm{sgn}(e_s)\boldsymbol{y}^{(2)}\right) + \Delta\varepsilon_h\left(\frac{1}{\eta_2}\frac{d\varepsilon_h}{dt} - p_2\mathrm{sgn}(e_s)\right)\end{aligned} \tag{51}$$

Substituting (46) and (47) into (51), the time derivative of V_{c1} can be expressed as

$$\frac{dV_{c1}}{dt} = -p_1 p_2 \sqrt{|e_s|} \le 0 \tag{52}$$

Since the time derivative of V_{c1} is negative semidefinite, the following inequality can be derived.

$$V_{c1}\left(e_s(t), \phi_2(t), \Delta \boldsymbol{W}(t), \varepsilon_h(t)\right) \le V_{c1}\left(e_s(0), \phi_2(0), \Delta \boldsymbol{W}(0), \varepsilon_h(0)\right) \tag{53}$$

According to (53), $e_s(t)$, $\phi_2(t)$, $\Delta W_i(t)$ and $\varepsilon_h(t)$ are bounded. Based on (52) and (53), the following function is defined.

$$\Omega_c(t) = -p_1 p_2 \sqrt{|e_s(t)|} \le -\frac{d}{dt} V_{c1}\left(e_s(t), \phi_2(t), \Delta \boldsymbol{W}(t), \varepsilon_h(t)\right) \tag{54}$$

Combining (54) with (53), the following inequality can be derived.

$$\int_0^t \Omega_c(\tau) d\tau \le V_{c1}\left(e_s(0), \phi_2(0), \Delta \boldsymbol{W}(0), \varepsilon_h(0)\right) - V_{c1}\left(e_s(t), \phi_2(t), \Delta \boldsymbol{W}(t), \varepsilon_h(t)\right) \tag{55}$$

Since $V_{c1}(e_s(0), \phi_2(0), \Delta \boldsymbol{W}(0), \varepsilon_h(0))$ is bounded and $V_{c1}(e_s(t), \phi_2(t), \Delta \boldsymbol{W}(t), \varepsilon_h(t))$ is a non-increasing bounded function, the following inequality can be derived.

$$\lim_{t \to \infty} \int_0^t \Omega_c(\tau) d\tau < \infty \tag{56}$$

Since $\lim_{t\to\infty} \int_0^t \Omega_c(\tau) d\tau$ exists and $\Omega_c(t)$ is a uniformly continuous function, according to Barbălat's Lemma [65], $\lim_{t\to\infty} \Omega_c(t) = 0$ holds. It means that $\lim_{t\to\infty} e_s(t) = 0$ holds. Therefore, the origin is a globally asymptotically stable equilibrium point of the system (45). The proof is completed. ■

The system (43) can be converted to another equivalent system described as

$$\frac{de_s}{dt} = -p_1 \sqrt{|e_s|} \operatorname{sgn}(e_s) + \phi_3, \quad \frac{d\phi_3}{dt} = -p_2 \operatorname{sgn}(e_s) + \rho_3(x,t) \tag{57}$$

where $\rho_3(x,t)$ is expressed as

$$\rho_3 = \frac{d}{dt}\left(-\Delta \boldsymbol{W}^T \boldsymbol{y}^{(2)} - \Delta \varepsilon_h\right) = -\boldsymbol{y}^{(2)T} \frac{d\boldsymbol{W}}{dt} - \Delta \boldsymbol{W}^T \frac{d\boldsymbol{y}^{(2)}}{dt} - \frac{d\varepsilon_h}{dt} = -\eta_1 p_2 \operatorname{sgn}(e_s) \boldsymbol{y}^{(2)T} \boldsymbol{y}^{(2)} - \Delta \boldsymbol{W}^T \frac{d\boldsymbol{y}^{(2)}}{dt} - \eta_2 p_2 \operatorname{sgn}(e_s) \tag{58}$$

Assumption 2 The time derivative of e_s is bounded.

Since ΔW_i, e_s and it time derivative are bounded, based on (22), (23) and (26), $y_i^{(2)}$ and its time derivative are bounded. Thus, ρ_3 is bounded.

In order to ensure the globally finite-time stability of the system (57), based on Theorem 1, the following Theorem is derived to select p_1 and p_2 for the proposed composite control law.

Theorem 3 *Considering the system* (57), *suppose* ρ_3 *is bounded as* (59) *for a positive constant* δ_2 *and the Lyapunov candidate function* V_{c2} *designed as* (60) *is used to perform the stability analysis*. *Then, if* p_1 *and* p_2 *are selected as* (61), *the origin is a globally finite-time-stable equilibrium point. Moreover, the corresponding settling-time function* T_2 *for the finite-time convergence of all trajectories of the system (57) to the origin is upper bounded by* (62).

$$|\rho_3| \le \delta_2 \tag{59}$$

$$V_{c2} = \zeta^T P \zeta \tag{60}$$

$$p_1 > 8, \quad p_2 > \frac{4p_1 + \delta_2}{4(p_1 - 8)} \tag{61}$$

$$T_2 \le \frac{2\sqrt{V_{c2}(\zeta_0)}}{q_2} \tag{62}$$

where $\zeta = [\sqrt{|e_s|}\mathrm{sgn}(e_s),\ \phi_3]^T$, ζ_0 is the initial condition of ζ, q_2 is related to p_1, p_2 and ρ_3.

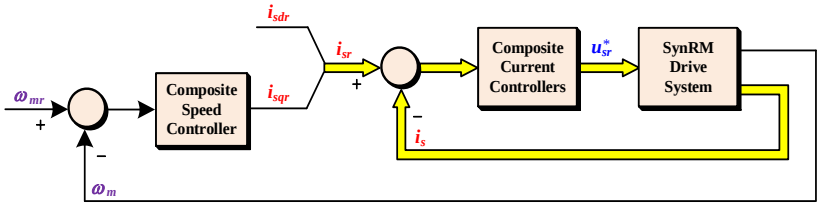

Fig. 4 Block diagram of the cascaded control structure adopted by the proposed HNN-SOSM control strategy.

Proof It can be observed that the system (57) has the same structure as the system (35) and V_{c2} can be obtained from V_{c1} by replacing ξ with ζ. Since ρ_3 is bounded as (59), the inequalities (61) can be obtained from (38) by replacing δ_1 with δ_2. Therefore, according to Theorem 1, it can be concluded that, with p_1 and p_2 selected as (61), the globally finite-time stability of the system (57) with the settling-time function upper bounded as (62) is guaranteed. The proof is completed. ■

5 Proposed HNN-SOSM control strategy

The cascaded control structure comprising the speed control loop and the current control loop is adopted by the proposed HNN-SOSM control strategy to accomplish the control objectives, as illustrated in Fig. 4, where $\boldsymbol{u}_{sr}^* = [u_{sdr}^*,\ u_{sqr}^*]^T$, $\boldsymbol{i}_{sr} = [i_{sdr},\ i_{sqr}]^T$ and $\boldsymbol{i}_s = [i_{sd},\ i_{sq}]^T$ are the reference stator voltage vector, the reference and the measured stator current vectors in the rotor reference frame, respectively. In the speed control loop, the proposed composite speed controller is used to let ω_m track ω_{mr}. In the current control loop, two composite current controllers, each of which comprises two standard STA-SOSM controllers, are employed to let i_{sd} and i_{sq} track i_{sdr} and i_{sqr}, respectively. i_{sdr} is kept at a constant value to excite the SynRM and i_{sqr} is generated by the composite speed controller. Since the dynamics of the current control loop is much faster than that of the speed control loop, the composite speed controller and the composite current controllers are designed separately.

5.1 Composite speed controller design

The tracking error for the rotor mechanical angular speed is defined as

$$e_\omega = \omega_{mr} - \omega_m \tag{63}$$

where e_ω denotes the tracking error for the rotor mechanical angular speed.

Based on (17) and (63), the dynamics of e_ω can be calculated as

$$\frac{de_\omega}{dt} = \underbrace{\frac{d\omega_{mr}}{dt} + \frac{1}{J}T_l + \frac{1}{J}T_f}_{\varphi_\omega} - \underbrace{\frac{3n_p}{2J}\left(L_d - L_q\right)i_{sd}}_{g_\omega} i_{sq} = \varphi_\omega - g_\omega i_{sq} \tag{64}$$

Considering external disturbances and parametric uncertainties presented in (19) and (20), the dynamics of e_ω can be rewritten as

$$\frac{de_\omega}{dt} = \varphi_\omega - \left(g_{\omega 0} + \Delta g_\omega\right)\left(i_{sq} + i_{sqr} - i_{sqr}\right) = \gamma_\omega - g_{\omega 0} i_{sqr} \tag{65}$$

where $g_{\omega 0}$ and Δg_{ω} denote nominal value and parametric uncertainties of g_{ω}, respectively, and $\gamma_{\omega} = \varphi_{\omega} - \Delta g_{\omega 0} i_{sqr} - (g_{\omega 0} + \Delta g_{\omega})(i_{sq} - i_{sqr})$ represents the lumped disturbance.

Selecting e_{ω} as the sliding variable, the proposed composite speed control law i_{sqr} is designed as

$$i_{sqr} = \mu_{\omega} + y_{h\omega} + y_{c\omega} \tag{66}$$

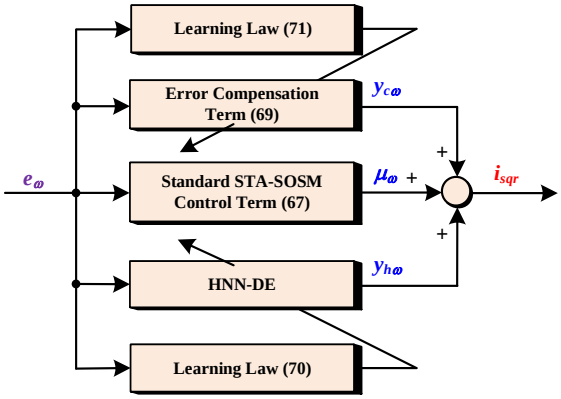

Fig. 5 Block diagram of the proposed composite speed controller.

$$\mu_{\omega} = \frac{1}{g_{\omega 0}}\left(p_{\omega 1}\sqrt{|e_{\omega}|}\,\mathrm{sgn}(e_{\omega}) + p_{\omega 2}\int \mathrm{sgn}(e_{\omega})\,dt\right) \tag{67}$$

$$y_{h\omega} = \frac{\boldsymbol{W}_{\omega}^{T}\boldsymbol{y}_{\omega}^{(2)}}{g_{\omega 0}} \tag{68}$$

$$y_{c\omega} = \frac{\varepsilon_{h\omega}}{g_{\omega 0}} \tag{69}$$

where μ_{ω}, $y_{h\omega}$ and $y_{c\omega}$ denote the standard STA-SOSM control term, the HNN-DE term and the error compensation term in the proposed composite control law, respectively, $p_{\omega 1}$ and $p_{\omega 2}$ are positive constant gains, $\boldsymbol{y}_{\omega}^{(2)} = [y_{\omega 1}^{(2)}, y_{\omega 2}^{(2)}, y_{\omega 3}^{(2)}, y_{\omega 4}^{(2)}, y_{\omega 5}^{(2)}]^{T}$ and $\boldsymbol{W}_{\omega} = [W_{\omega 1}\ W_{\omega 2}\ W_{\omega 3}\ W_{\omega 4}\ W_{\omega 5}]^{T}$ are the output signal vector of the hidden layer and the output weight vector of the adopted HNN-DE, respectively $\varepsilon_{h\omega}$ is the estimated minimum approximation error for the adopted HNN-DE.

Remark 2 If the HNN-DE term and the error compensation term are removed, the proposed composite speed control law is turned into the standard STA-SOSM speed control law, which is expressed as (67).

With regard to the HNN-DE adopted by the proposed composite speed control law, e_{ω} is selected as the input signal. Therefore, the learning laws for $\boldsymbol{W}_{\omega}$ and $\varepsilon_{h\omega}$ are designed as

$$\frac{d\boldsymbol{W}_{\omega}}{dt} = \eta_{\omega 1} p_{\omega 2}\mathrm{sgn}(e_{\omega})\boldsymbol{y}_{\omega}^{(2)} \tag{70}$$

$$\frac{d\varepsilon_{h\omega}}{dt} = \eta_{\omega 2} p_{\omega 2}\mathrm{sgn}(e_{\omega}) \tag{71}$$

where $\eta_{\omega 1}$ and $\eta_{\omega 2}$ are positive learning rates.

Substituting (66) into (65), the dynamics of e_{ω} using the proposed composite speed control law can be expressed as

$$\begin{aligned}\frac{de_{\omega}}{dt} &= -p_{\omega 1}\sqrt{|e_{\omega}|}\,\mathrm{sgn}(e_{\omega}) - p_{\omega 2}\int \mathrm{sgn}(e_{\omega})\,dt \underbrace{-\boldsymbol{W}_{\omega}^{T}\boldsymbol{y}_{\omega}^{(2)} - \varepsilon_{h\omega} + \gamma_{\omega}}_{\rho_{\omega}} \\ &= -p_{\omega 1}\sqrt{|e_{\omega}|}\,\mathrm{sgn}(e_{\omega}) - p_{\omega 2}\int \mathrm{sgn}(e_{\omega})\,dt + \rho_{\omega}\end{aligned} \tag{72}$$

Assumption 3 There are positive constants $\delta_{\omega 1}$ and $\delta_{\omega 2}$ such that ρ_ω and its time derivative $\dot{\rho}_\omega$ are bounded as $|\rho_\omega| \le \delta_{\omega 1}$ and $|\dot{\rho}_\omega| \le \delta_{\omega 2}$.

Considering Assumption 3, based on Theorem 2 and Theorem 3, it can be concluded that, with the proposed composite speed control law (66) as well as learning laws (70) and (71), e_ω will converge to the origin in a finite time if $p_{\omega 1}$ and $p_{\omega 2}$ are selected as

$$p_{\omega 1} > 8, \quad p_{\omega 2} > \frac{4p_{\omega 1} + \delta_{\omega 2}}{4(p_{\omega 1} - 8)} \tag{73}$$

The block diagram of the proposed composite speed controller is shown in Fig. 5.

5.2 Composite current controller design

The tracking errors for direct and quadrature axes stator current components are defined as

$$e_d = i_{sdr} - i_{sd}, \quad e_q = i_{sqr} - i_{sq} \tag{74}$$

where e_d and e_q denote the tracking errors for direct and quadrature axes stator current components, respectively.

According to (17), the dynamics of i_{sd} and i_{sq} can be described as

$$\frac{di_{sd}}{dt} = g_{qq}\left(u_{sd}^* + u_{sd}^d - \varphi_{dd}\right) - g_{dq}\left(u_{sq}^* + u_{sq}^d - \varphi_{qq}\right), \quad \frac{di_{sq}}{dt} = -g_{qd}\left(u_{sd}^* + u_{sd}^d - \varphi_{dd}\right) + g_{dd}\left(u_{sq}^* + u_{sq}^d - \varphi_{qq}\right) \tag{75}$$

where

$$g_{dd} = \frac{L_{dd}}{M}, \quad g_{dq} = \frac{L_{dq}}{M}, \quad g_{qd} = \frac{L_{qd}}{M}, \quad g_{qq} = \frac{L_{qq}}{M}, \quad \varphi_{dd} = R_s i_{sd} - n_p \omega_m L_q i_{sq}, \quad \varphi_{qq} = R_s i_{sq} + n_p \omega_m L_d i_{sd}$$

Considering parametric uncertainties presented in (19) and (20), the dynamics of i_{sd} and i_{sq} can be rewritten as

$$\begin{cases} \dfrac{di_{sd}}{dt} = \left(g_{qq0} + \Delta g_{qq}\right)\left(u_{sd}^* + u_{sd}^d - \varphi_{dd0} - \Delta\varphi_{dd}\right) - \left(g_{dq0} + \Delta g_{dq}\right)\left(u_{sq}^* + u_{sq}^d - \varphi_{qq0} - \Delta\varphi_{qq}\right) \\ \dfrac{di_{sq}}{dt} = -\left(g_{qd0} + \Delta g_{qd}\right)\left(u_{sd}^* + u_{sd}^d - \varphi_{dd0} - \Delta\varphi_{dd}\right) + \left(g_{dd0} + \Delta g_{dd}\right)\left(u_{sq}^* + u_{sq}^d - \varphi_{qq0} - \Delta\varphi_{qq}\right) \end{cases} \tag{76}$$

where Δg_{dd}, Δg_{dq}, Δg_{qd}, Δg_{qq}, $\Delta\varphi_{dd}$, and $\Delta\varphi_{qq}$ represent parametric uncertainties in respect of g_{dd}, g_{dq}, g_{qd}, g_{qq}, φ_{dd}, and φ_{qq}, respectively, g_{dd0}, g_{dq0}, g_{qd0}, g_{qq0}, φ_{dd0}, and φ_{qq0} are nominal values of g_{dd}, g_{dq}, g_{qd}, g_{qq}, φ_{dd}, and φ_{qq}, respectively, which are expressed as

$$g_{dd0} = \frac{L_{dd0}}{M_0}, \quad g_{dq0} = \frac{L_{dq0}}{M_0}, \quad g_{qd0} = \frac{L_{qd0}}{M_0}, \quad g_{qq0} = \frac{L_{qq0}}{M_0}$$
$$M_0 = L_{dd0}L_{qq0} - L_{dq0}L_{qd0}, \quad \varphi_{dd0} = R_{s0} i_{sd} - n_p \omega_m L_{q0} i_{sq}, \quad \varphi_{qq0} = R_{s0} i_{sq} + n_p \omega_m L_{d0} i_{sd}$$

According to (74) and (76), the dynamics of e_d and e_q can be described as

$$\frac{de_d}{dt} = -g_{qq0}\left(u_{sdr}^* - \varphi_{dd0}\right) + g_{dq0}\left(u_{sqr}^* - \varphi_{qq0}\right) + \gamma_d, \quad \frac{de_q}{dt} = g_{qd0}\left(u_{sdr}^* - \varphi_{dd0}\right) - g_{dd0}\left(u_{sqr}^* - \varphi_{qq0}\right) + \gamma_q \tag{77}$$

where γ_d and γ_q represent lumped disturbances expressed as

$$\begin{cases} \gamma_d = -g_{qq}\left(u_{sd}^* - u_{sdr}^* + u_{sd}^d - \Delta\varphi_{dd}\right) + g_{dq}\left(u_{sq}^* - u_{sqr}^* + u_{sq}^d - \Delta\varphi_{qq}\right) - \Delta g_{qq}\left(u_{sdr}^* - \varphi_{dd0}\right) + \Delta g_{dq}\left(u_{sqr}^* - \varphi_{qq0}\right) + \dfrac{di_{sdr}}{dt} \\ \gamma_q = g_{qd}\left(u_{sd}^* - u_{sdr}^* + u_{sd}^d - \Delta\varphi_{dd}\right) - g_{dd}\left(u_{sq}^* - u_{sqr}^* + u_{sq}^d - \Delta\varphi_{qq}\right) + \Delta g_{qd}\left(u_{sdr}^* - \varphi_{dd0}\right) - \Delta g_{dd}\left(u_{sqr}^* - \varphi_{qq0}\right) + \dfrac{di_{sqr}}{dt} \end{cases}$$

Assumption 4 There are positive constants δ_{d1}, δ_{d2}, δ_{q1}, δ_{q2} such that γ_d, γ_q and their time derivatives $\dot{\gamma}_d$ and $\dot{\gamma}_q$ are bounded as $|\gamma_d| \le \delta_{d1}$, $|\gamma_q| \le \delta_{q1}$, $|\dot{\gamma}_d| \le \delta_{d2}$, and $|\dot{\gamma}_q| \le \delta_{q2}$.

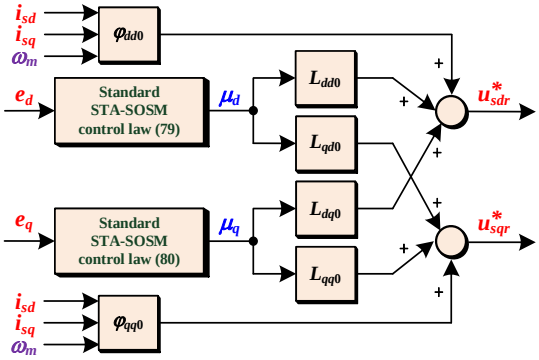

Fig. 6 Block diagram of the proposed composite current controllers.

Selecting e_d and e_q as the sliding variables, two proposed composite current control laws u_{sdr} and u_{sqr} are designed as

$$u^*_{sdr} = \varphi_{dd0} + L_{dd0}\mu_d + L_{dq0}\mu_q, \quad u^*_{sqr} = \varphi_{qq0} + L_{qd0}\mu_d + L_{qq0}\mu_q \tag{78}$$

where μ_d and μ_q are two standard STA-SOSM control laws expressed as (79) and (80), respectively.

$$\mu_d = p_{d1}\sqrt{|e_d|}\,\mathrm{sgn}(e_d) + p_{d2}\int \mathrm{sgn}(e_d)\,dt \tag{79}$$

$$\mu_q = p_{q1}\sqrt{|e_q|}\,\mathrm{sgn}(e_q) + p_{q2}\int \mathrm{sgn}(e_q)\,dt \tag{80}$$

where p_{d1}, p_{d2}, p_{q1}, p_{q2} are positive constant gains.

Substituting (78) into (77), the dynamics of e_d and e_q using the proposed composite current control laws can be expressed as

$$\frac{de_d}{dt} = -p_{d1}\sqrt{|e_d|}\,\mathrm{sgn}(e_d) - p_{d2}\int \mathrm{sgn}(e_d)\,dt + \gamma_d, \quad \frac{de_q}{dt} = -p_{q1}\sqrt{|e_q|}\,\mathrm{sgn}(e_q) - p_{q2}\int \mathrm{sgn}(e_q)\,dt + \gamma_q \tag{81}$$

Considering Assumption 4, according to Theorem 1, it can be concluded that, with the proposed composite current control laws (78), e_d and e_q will converge to the origin in a finite time if p_{d1}, p_{d2}, p_{q1}, p_{q2} are selected as

$$p_{d1} > 8, \quad p_{d2} > \frac{4p_{d1} + \delta_{d2}}{4(p_{d1} - 8)}, \quad p_{q1} > 8, \quad p_{q2} > \frac{4p_{q1} + \delta_{q2}}{4(p_{q1} - 8)} \tag{82}$$

The block diagram of the proposed composite current controllers are shown in Fig. 6.

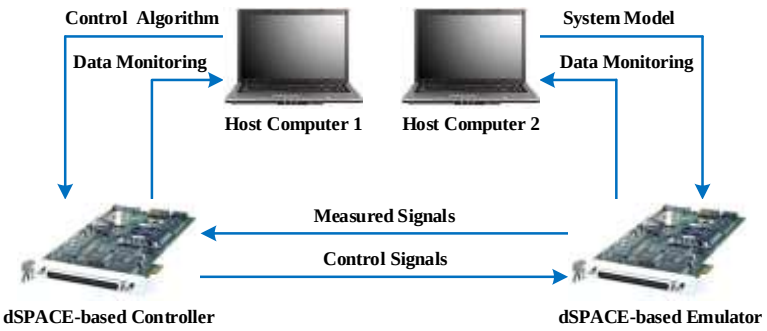

Fig. 7 Block diagram of the HIL test bench.

6. HIL test results

To perform comparative tests between the proposed HNN-SOSM control strategy and the conventional STA-SOSM control strategy, a HIL test bench based on two dSPACE is built, as presented

in Fig. 7. It is a cost-effective real-time verification platform to test the control strategy [34, 66, 67]. There are two dSPACE DS1104 Research and Development Boards in the HIL test bench: one is used as the hardware controller to implement the tested vector control strategies, where the sampling frequency is 5 kHz, the other is employed as the emulator to emulate the 2L-VSI-fed SynRM drive system, where the sampling frequency is 10 kHz. With regard to the emulator, it adopts the low-frequency model of the 2L-VSI presented in (9) and the dynamic model of the SynRM presented in (17). Moreover, the Park's transformation and its inverse form are used to achieve the transformation of stator voltage and current components between the three-phase stator reference frame and the rotor reference frame. With regard to the hardware controller, it generates d_a^*, d_b^* and d_c^* for the 2L-VSI in the emulator, which is based on the space-vector modulation, and samples i_{an}, i_{bn}, i_{cn} and rotor mechanical position θ_m from the emulator, as illustrated in Fig. 8.

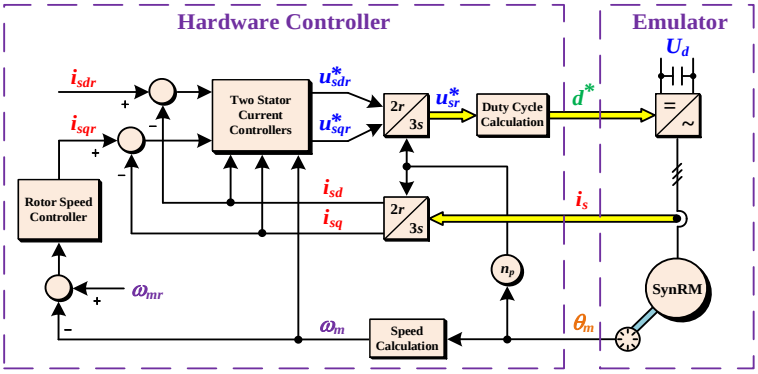

Fig. 8 Block diagram of the implementation of the vector-controlled SynRM drive system in HIL tests.

Table 1 Parameters of the SynRM

Parameter	Value
Nominal stator resistance, R_{s0}	1.05 Ω
Nominal angular speed, ω_{mn}	1500 rpm
Nominal torque, T_{rn}	4.8 N·m
Nominal rotor inertia, J_0	2.08 × 10^{-2} kg·m^2
Nominal viscous friction coefficient, B_{mn}	2.68 × 10^{-3} N·m·s/rad
Pole pairs, n_p	2

Table 2 Specifications of the 2L-VSI

Parameter	Value
DC-bus voltage, U_d	200 V
Switching period, T_s	100 μs
Turn-on time, T_{on}	1.3 μs
Turn-off time, T_{off}	1.3 μs
Dead time, T_{dead}	2.0 μs
Saturation voltage, U_{sat}	1.6 V
Diode forward voltage, U_{diode}	1.5 V

The parameters of the SynRM are presented in Table 1 [15]. The specifications of the 2L-VSI are shown in Table 2 [49]. The adopted apparent inductance model of the SynRM is illustrated in Fig. 9, whose parameters are presented as follow: $c_{d1} = 0.0391$, $c_{d2} = 45.4$, $c_{d3} = -12.9$, $c_{d4} = 1329$, $c_{d5} = 19.9$, $c_{d6} = -13$, $c_{d7} = 795$, $c_{dq} = 0.0133$, $c_{q1} = 0.01$, $c_{q2} = 0.571$, $c_{q3} = 0$, $c_{q4} = 58$, $c_{q5} = 0.825$, $c_{q6} = 0$, $c_{q7} = 63.8$, $c_{qd} = 0.0833$ [14]. With respect to the proposed HNN-SOSM control strategy, the parameters of the composite speed controller are selected as $L_{d0} = L_d(0,0)$, $L_{q0} = L_q(0,0)$, $p_{\omega 1} = 100$,

$p_{\omega 2} = 200$, $\eta_{\omega 1} = 100$, $\eta_{\omega 2} = 0.1$, and the parameters of two composite current controllers are selected as $L_{d0} = L_d(0,0)$, $L_{q0} = L_q(0,0)$, $L_{dd0} = L_{dd}(1,1)$, $L_{dq0} = L_{dq}(1,1)$, $L_{qd0} = L_{qd}(1,1)$, $L_{qq0} = L_{qq}(1,1)$, $p_{d1} = p_{q1} = 5000$, $p_{d2} = p_{q2} = 20000$. With respect to the conventional STA-SOSM control strategy, the parameters of the standard STA-SOSM speed controller are selected as $L_{d0} = L_d(0,0)$, $L_{q0} = L_q(0,0)$, $p_{\omega 1} = 100$, $p_{\omega 2} = 200$, and the parameters of two PI current controllers are the same as each other, i.e., the proportional gain is selected as 30 and the integral gain is selected as 4000. Regarding the implementation of STA-based controllers in the hardware controller, the sign function is usually replaced by the saturation function [68] or the hyperbolic tangent function [69] to further alleviate the chattering phenomenon. Therefore, in this paper, the sign function in STA-based controllers is replaced by the following saturation function in HIL tests

$$\mathrm{sat}(e_s) = \begin{cases} e_s / l, & \text{if } |e_s| \le l \\ \mathrm{sign}(e_s), & \text{if } |e_s| > l \end{cases} \tag{83}$$

where l denotes the boundary layer and its value is selected as 1 in this paper.

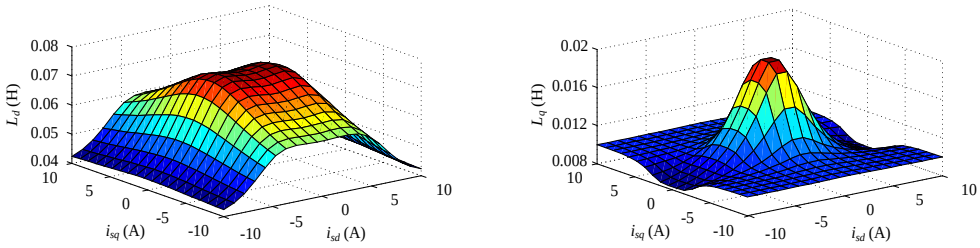

(a) (b)

Fig. 9 Apparent inductance maps of the SynRM. (a) L_d (i_{sd}, i_{sq}), (b) L_q (i_{sd}, i_{sq})

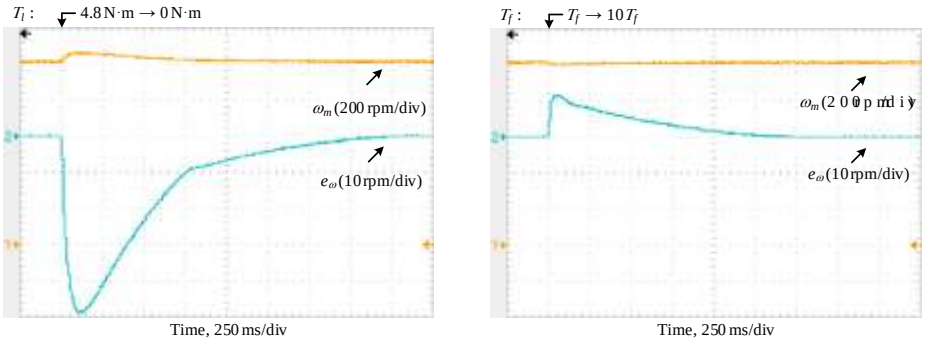

(a)

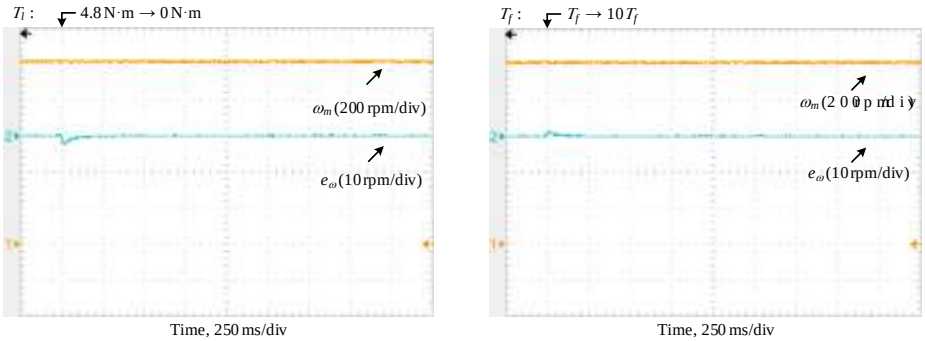

(b)

Fig. 10 Speed responses for the first test. (a) Conventional STA-SOSM control strategy. (b) Proposed HNN-SOSM control strategy

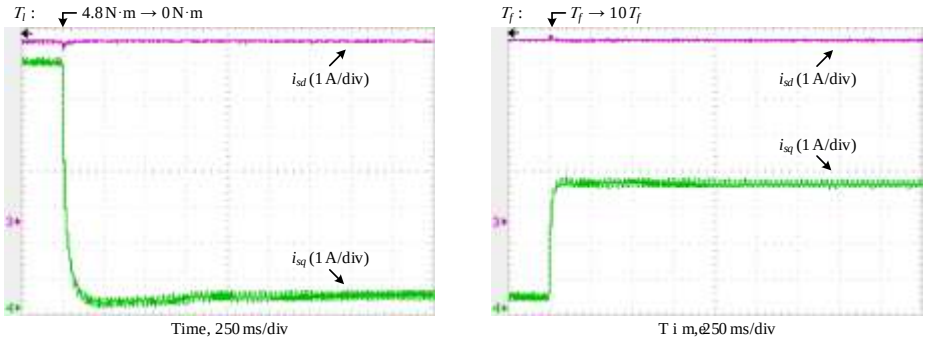

(a)

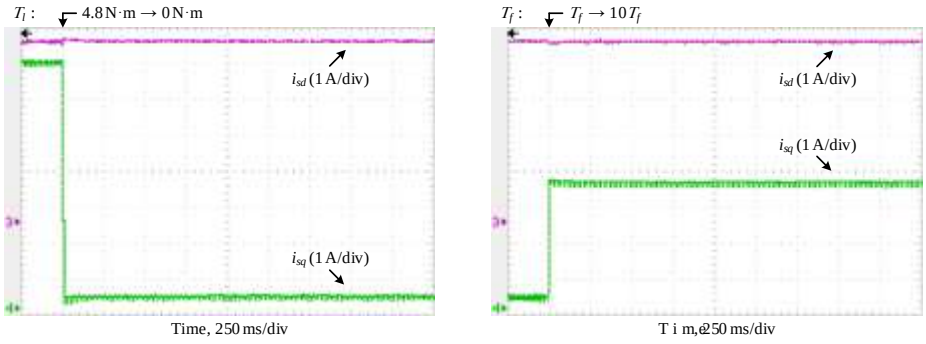

(b)

Fig. 11 Current responses for the first test. (a) Conventional STA-SOSM control strategy. (b) Proposed HNN-SOSM control strategy

In the first test, the values of ω_{mr}, i_{sdr}, ΔJ and ΔR_s are set to 1000 rpm, 5 A, 0 and 0, respectively. The value of T_l declines from 4.8 N·m to 0 N·m at first, and then the value of T_f steps tenfold by raising the value of B_m to ten times. Fig. 10 presents the speed responses of the proposed HNN-SOSM control strategy and the conventional STA-SOSM control strategy, while the current responses of these two tested control strategies are illustrated in Fig. 11. It can be seen that, in comparison with the conventional STA-SOSM control strategy, the proposed HNN-SOSM control strategy can achieve smaller maximum tracking error and shorter settling time for the speed and current tracking control under the sudden change of external disturbances.

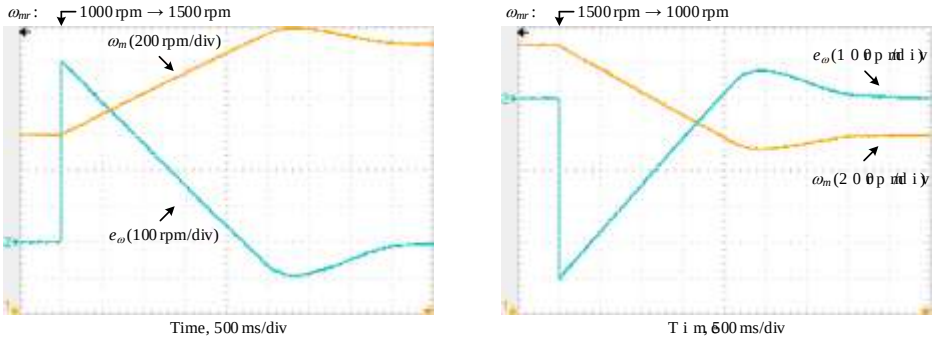

(a)

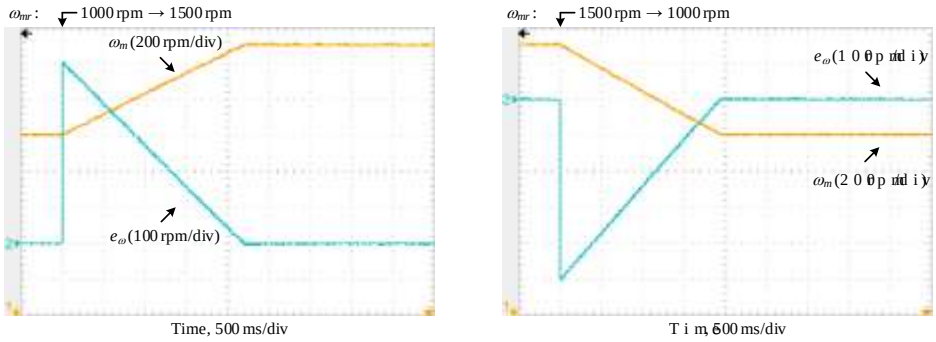

(b)

Fig. 12 Speed responses for the second test. (a) Conventional STA-SOSM control strategy. (b) Proposed HNN-SOSM control strategy

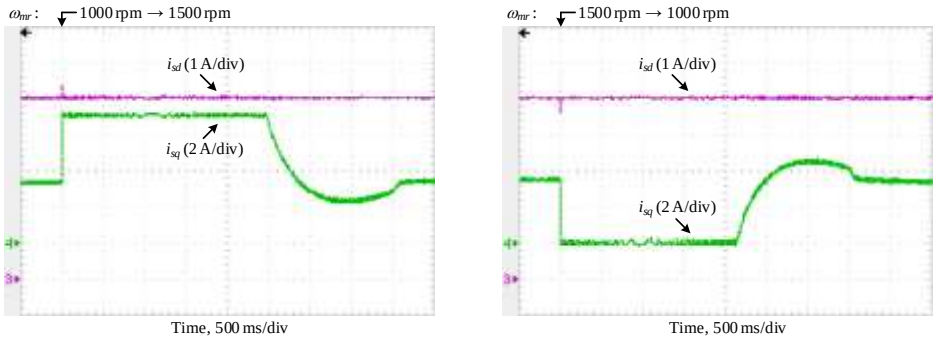

(a)

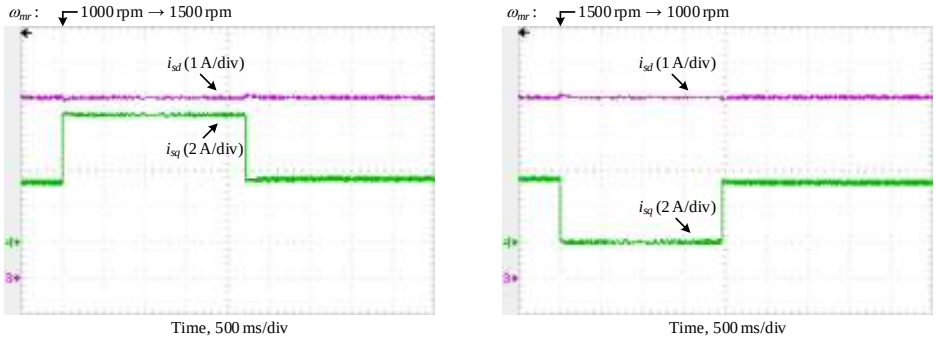

(b)

Fig. 13 Current responses for the second test. (a) Conventional STA-SOSM control strategy. (b) Proposed HNN-SOSM control strategy

In the second test, the values of T_l, i_{sdr}, ΔJ and ΔR_s are set to 2.4 N·m, 5 A, $4J_0$ and 0, respectively. The value of ω_{mr} steps from 1000 rpm to 1500 rpm at first, and then it is back to 1000 rpm. The speed and current responses of two tested control strategies are presented in Fig. 12 and Fig. 13, respectively. It can be observed that, in the presence of the rotor inertia uncertainty, the proposed HNN-SOSM control strategy can accomplish smaller overshoot and shorter settling time for the speed and current tracking control under the sudden change of the reference rotor mechanical angular speed, compared with the conventional STA-SOSM control strategy.

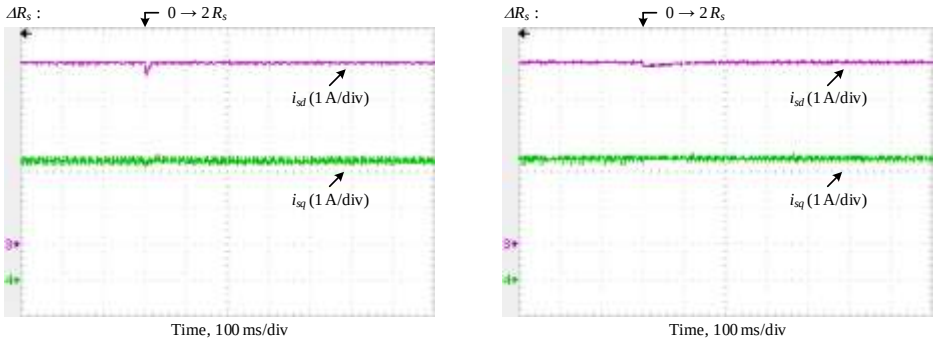

Fig. 14 Current responses for the third test. (a) Conventional STA-SOSM control strategy. (b) Proposed HNN-SOSM control strategy

In the third test, the values of ω_{mr}, T_l, i_{sdr} and ΔJ are set to 1000 rpm, 2.4 N·m, 5 A and 0, respectively, while the value of ΔR_s steps from 0 to $2R_s$. The current responses of two tested control strategies are shown in Fig. 14. It can be seen that the variations of stator current components of the proposed HNN-SOSM control strategy is smaller than those of the conventional STA-SOSM vector control strategy.

7. Conclusions

In this paper, a novel robust dual-loop vector control strategy is proposed for the SynRM drive system, which is based on the cascaded control structure consisting of the speed control loop and the current control loop. The external disturbances and parametric uncertainties are considered in the controller design. In the speed control loop, a composite speed controller consisting of a standard STA-SOSM controller, a HNN-DE and an error compensator is designed to regulate the rotor angular speed. Moreover, the learning laws for the HNN-DE and the error compensator are derived by the Lyapunov synthesis approach. The rigorous stability analysis for the speed tracking error dynamics using the proposed composite speed controller is presented. In the current control loop, two composite current controllers, each of which is composed of two standard STA-SOSM controllers, are proposed to regulate direct and quadrature axes stator current components in the rotor reference frame. The rigorous stability analyses for the current tracking error dynamics using proposed composed current controllers are presented. The results of the HIL tests show that the SynRM drive system using the proposed HNN-SOSM control strategy is able to accomplish better tracking performance and higher robustness against external disturbances and parametric uncertainties in comparison with the SynRM drive system using the conventional STA-SOSM vector control strategy.

Declaration of Competing Interest

The authors declare that they have no known competing financial interests or personal relationships that could have appeared to influence the work reported in this paper.

Acknowledgments

This work was supported by the USP-SRT Research Project (ACOSREV).

References

[1] G. Pellegrino, T.M. Jahns, N. Bianchi, W.L. Soong, F. Cupertino, The Rediscovery of Synchronous Reluctance and Ferrite Permanent Magnet Motors, Springer, Basel, Switzerland, 2016.

[2] A. Vagati, The synchronous reluctance solution: a new alternative in AC drives, in: Proc. 20th Annu. Conf. IEEE Ind. Electron. Soc., Bologna, Italy, 1994, pp. 1-13.

[3] R. R. Moghaddam, F. Magnussen, C. Sadarangani, Theoretical and experimental reevaluation of synchronous reluctance machine, IEEE Trans. Ind. Electron. 57 (1) (2010) 6-13.

[4] S.M. Taghavi, P. Pillay, A mechanically robust rotor with transverse laminations for a wide-speed-range synchronous reluctance traction motor, IEEE Trans. Ind. Appl. 51 (6) (2015) 4404-4414.

[5] V. Bilyi, D. Gerling, Synchronous reluctance machine with integer-slot double-layer concentrated winding for wind energy applications, in: Proc. 4th IEEE Int. Conf. Smart Energy Grid Eng., Oshawa, Canada, 2016, pp. 111-116.

[6] N. Bianchi, S. Bolognani, E. Carraro, M. Castiello, E. Fornasiero, Electric vehicle traction based on synchronous reluctance motors, IEEE Trans. Ind. Appl. 52 (6) (2016) 4762-4769.

[7] M.N. Ibrahim, H. Rezk, M. Al-Dhaifallah, P. Sergeant, Solar array fed synchronous reluctance motor driven water pump: an improved performance under partial shading conditions, IEEE Access 7 (2019) 77100-77115.

[8] A. Varshney, U. Sharma, B. Singh, Self-regulated DC-link control of synchronous reluctance motor-driven solar water pumping system, IET Power Electron. 12 (12) (2019) 1-11.

[9] G. V. Kumar, C. -H. Chuang, M. -Z. Lu, C. -M. Liaw, Development of an electric vehicle synchronous reluctance motor drive, IEEE Trans. Veh. Technol. 69 (5) (2020) 5012-5024.

[10] Y. -C. Liu, S. Laghrouche, A. N'Diaye, S. Narayan, G. Cirrincione, M. Cirrincione, Sensorless control of synchronous reluctance motor drives based on the TLS EXIN neuron, in: Proc. IEEE Int. Electr. Mach. Drives Conf., San Diego, USA, 2019, pp. 1737-1741.

[11] A. Varatharajan, G. Pellegrino, Sensorless synchronous reluctance motor drives: a general adaptive projection vector approach for position estimation, IEEE Trans. Ind. Appl. 56 (2) (2020) 1495-1503.

[12] M.-Y. Mei, T.-H. Liu, Design and implementation of an online tuning adaptive controller for synchronous reluctance motor drives, IEEE Trans. Ind. Electron. 60 (9) (2013) 3644-3657.

[13] J. Yang, W.-H. Chen, S. Li, L. Guo, Y. Yan, Disturbance/uncertainty estimation and attenuation techniques in PMSM drives-a survey, IEEE Trans. Ind. Electron. 64 (4) (2017) 3273-3285.

[14] S. Yamamoto, K. Tomishige, T. Ara, Maximum efficiency operation of vector-controlled synchronous reluctance motors considering cross-magnetic saturation, IEEJ Trans. Ind. Appl. 126 (7) (2006) 1021–1027.

[15] S. Yamamoto, T. Ara, K. Matsuse, A method to calculate transient characteristics of synchronous reluctance motors considering iron loss and cross-magnetic saturation, IEEE Trans. Ind. Appl. 43 (1) (2007) 47–56.

[16] E. Armando, R.I. Bojoi, P. Guglielmi, G. Pellegrino, M. Pastorelli, Experimental identification of the magnetic model of synchronous machines, IEEE Trans. Ind. Appl. 49 (5) (2013) 2116-2125.

[17] S. Wiedemann, S. Hall, R. M. Kennel, M. Alaküla, Dynamic testing characterization of a synchronous reluctance machine, IEEE Trans. Ind. Appl. 54 (2) (2018) 1370-1378.

[18] C.-H. Lin, K.-T. Chang, Admixed recurrent Gegenbauer polynomials neural network with mended particle swarm optimization control system for synchronous reluctance motor driving continuously variable transmission system, Proc. Inst. Mech. Eng. Pt. I: J. Syst. Contr. Eng. 234 (2) (2020) 1-16.

[19] F.-J. Lin, M.-S. Huang, S.-G. Chen, C.-W. Hsu, C.-H. Liang, Adaptive backstepping control for synchronous reluctance motor based on intelligent current angle control, IEEE Trans. Power Electron. 35 (7) (2020) 7465-7479.

[20] H.A. Zarchi, J. Soltani, G.A. Markadeh, Adaptive input-output feedback-linearization-based torque control of synchronous reluctance motor without mechanical sensor, IEEE Trans. Ind. Electron. 57 (1) (2010) 375-384.

[21] C.-K. Lin, J.-T. Yu, Y.-S. Lai, H.-C. Yu, Improved model-free predictive current control for synchronous reluctance motor drives, IEEE Trans. Ind. Electron. 63 (6) (2016) 3942-3953.

[22] Y.-C. Liu, S. Laghrouche, A. N'Diaye, and M. Cirrincione, Model predictive current and capacitor voltage control of post-fault three-level NPC inverter-fed synchronous reluctance motor drives, in: Proc. Int. Aegean Conf. Electr. Mach. Power Electron. & Intl Conf. Optim. Electr., Electron. Equip., Istanbul, Turkey, 2019, pp. 221-226.

[23] I. Boldea, N. Muntean, S.A. Nsasr, Robust low-cost implementation of vector control for reluctance synchronous machines, IEE Proc.-Electr. Power Appl. 141 (1) (1993) 1-6.

[24] K.-K. Shyu, C.-K. Lai, Incremental motion control of synchronous reluctance motor via multisegent sliding mode control method, IEEE Trans. Control Syst. Technol. 10 (2) (2002) 169-176.

[25] T. Sharaf-Eldin, M.W. Dunnigan, J.E. Fletcher, B.W. Williams, Nonlinear robust control of a vector-controller synchronous reluctance machine, IEEE Trans. Ind. Electron. 14 (6) (1999) 1111-1121.

[26] H.-K. Chiang, W.-B. Lin, Sub-optimal algorithm second-order sliding mode control for a synchronous reluctance motor speed drive, Trans. Can. Soc. Mech. Eng. 40 (5) (2016) 897–908.

[27] W.-B. Lin, H.-K. Chiang, 2013, Super-twisting algorithm second-order sliding mode control for a synchronous reluctance motor speed drive, Math. Probl. Eng. 13, 632061.

[28] V. Utkin, H. Lee, Chattering problem in sliding mode control systems, in: Proc. Int. Workshop Variable Structure Syst., Alghero, Italy, 2006, pp. 346-350.

[29] V. Utkin, J. Guldner, J.X. Shi, Sliding Mode Control in Electro-Mechanical Systems. CRC Press, Boca Raton, USA, 2009.

[30] Y. Shtessel, C. Edwards, L. Fridman, A. Levant, Sliding Mode Control and Observation. Birkhäuser, Basel, 2014.

[31] A. Levant, Sliding order and sliding accuracy in sliding mode control, Int. J. Control 58 (6) (1993) 1247-1263.

[32] A. Levant, Principles of 2-sliding mode design, Automatica 43 (4) (2007) 576-586.

[33] Y.B. Shtessel, J.A. Moreno, F. Plestan, L.M. Fridman, A.S. Poznyak, Super-twisting adaptive sliding mode control: a Lyapunov design, in: Proc. 49th IEEE Conf. Dec. Control, Atlanta, USA, 2010, pp. 5109–5113.

[34] L. Zhang, H. Zhang, H. Obeid, S. Laghrouche, Time-varying state observer based twisting control of linear induction motor considering dynamic end effects with unknown load torque, ISA Trans. 93 (2019) 290–301.

[35] C. Evangelista, P. Puleston, F. Valenciaga, L. M. Fridman, Lyapunov-designed super-twisting sliding mode control for wind energy conversion optimization, IEEE Trans. Ind. Electron. 60 (2) (2013) 538-545.

[36] C. Vázquez, J. Collado, L. Fridman, Super twisting control of a parametrically excited overhead crane, J. Frankl. Inst. 351 (4) (2014) 2283-2298.

[37] Z. Zhao, J. Yang, S. Li, Z. Zhang, L. Guo, Finite-time super-twisting sliding mode control for Mars entry trajectory tracking, J. Frankl. Inst. 352 (11) (2015) 5226-5248.

[38] J. Liu, Y. Yin, W. Luo, S. Vazquez, L. G. Franquelo, L. Wu, Sliding mode control of a three-phase AC/DC voltage source converter under unknown load conditions: industry applications, IEEE Trans. Syst., Man, Cybern. Syst. 48 (10) (2018) 1771-1780.

[39] R. Sadeghi, S.M. Madani, M. Ataei, M.R.A. Kashkooli, S. Ademi, Super-twisting sliding mode direct power control of a brushless doubly fed induction generator, IEEE Trans. Ind. Electron. 65 (11) (2018) 9147-9156.

[40] J. Davila, L. Fridman, A. Levant, Second-order sliding-mode observer for mechanical systems, IEEE Trans. Autom. Control 50 (11) (2005) 1785-1789.

[41] J. Liu, W. Luo, X. Yang, L. Wu, Robust model-based fault diagnosis for PEM fuel cell air-feed system, IEEE Trans. Ind. Electron. 63 (5) (2016) 3261-3270.

[42] B. Wang, Z. Dong, Y. Yu, G. Wang, and D. Xu, Static-errorless deadbeat predictive current control using second-order sliding-mode disturbance observer for induction machine drives, IEEE Trans. Power Electron. 33 (3) (2018) 2395-2403.

[43] H. Wang, X. Ge, Y.-C. Liu, Second-order sliding-mode MRAS observer based sensorless vector control of linear induction motor drives for medium-low speed maglev applications, IEEE Trans. Ind. Electron. 65 (12) (2018) 9938-9952.

[44] Y. Huangfu, S. Zhuo, F. Chen, S. Pang, D. Zhao, F. Gao, Robust voltage control of floating interleaved boost converter for fuel cell system, IEEE Trans. Ind. Appl. 54 (1) (2018) 665-674.

[45] J. A. Moreno, M. Osorio, A Lyapunov approach to second-order sliding mode controllers and observers, in: Proc. 47th IEEE Conf. Dec. Control, Cancun, Mexico, 2008, pp. 2856-2861.

[46] J. -W. Choi, S. -K. Sul, Inverter output voltage synthesis using novel dead time compensation, IEEE Trans. Power Electron. 11 (2) (1996) 221–227.

[47] K. Liu, Z. Q. Zhu, Online Estimation of the rotor flux linkage and voltage-source inverter nonlinearity in permanent magnet synchronous machine drives, IEEE Trans. Power Electron. 29 (1) (2014) 418–427.

[48] T. Qiu, X. Wen, F. Zhao, Adaptive-linear-neuron-based dead-time effects compensation scheme for PMSM drives, IEEE Trans. Power Electron. 31 (3) (2016) 2530–2538.

[49] Z. Tang, B. Akin, A new LMS algorithm based dead-time compensation method for PMSM FOC drives, IEEE Trans. Ind. Appl. 54 (6) (2018) 6472–6484.

[50] T. Fukuda, T. Shibata, Theory and applications of neural networks for industrial control systems, IEEE Trans. Ind. Electron. 39 (6) (1992) 472-489.

[51] Z. Feng, J. Fei, Super-twisting sliding mode control for micro gyroscope based on RBF neural network, IEEE Access 6 (2018) 64993-65001.

[52] A.-M. Zou, K.D Kumar, Z.-G. Hou, X. Liu, Finite-time attitude tracking control for spacecraft using terminal sliding mode and Chebyshev neural network, IEEE Trans. Syst., Man, Cybern. B, Cybern. 41 (4) (2011) 950–963.

[53] A. Kulkarni, V. Gupta, Tracking control for a class of uncertain nonlinear systems using Legendre neural network, in: Proc. Int. Conf. Informat. Commun. Embed Syst., Chennai, India, 2014, pp. 1–6.

[54] A. Zou, Y. Zhang, Basis Function Neural Networks and Their Applications, Sun Yat-sen University Press, Guangzhou, China, 2009.

[55] S. Gaglio, G. Pilato, F. Sorbello, G. Vassallo, Using the hermite regression formula to design a neural architecture with automatic learning of the "hidden" activation functions, Lect. Notes Comput. Sci. 1792 (1999) 226–237.

[56] M.R. Mackenzie, A.K. Tieu, Hermite neural network correlation and application, IEEE Trans. Signal Process. 51 (12) (2003) 3210–3219.

[57] L. Ma, K. Khorasani, Constructive feedforward neural network using Hermite polynomial activation functions, IEEE Trans. Neural Netw. 16 (4) (2005) 821–833.

[58] S.M. Siniscalchi, J. Li, C.-H. Lee, Hermite polynomial for speaker adaptation of connectionist speech recognition systems, IEEE Trans. Audio, Speech, Language Process. 21 (10) (2013) 2152–2161.

[59] F.-J Lin, S.-Y. Chen, M.-S. Huang, Tracking control of thrust active magnetic bearing via Hermite polynomial-based recurrent neural network, IET Electr. Power Appl. 4 (9) (2010) 701–714.

[60] S.-Y. Chen, F.-J Lin, Robust nonsingular terminal sliding-mode control for nonlinear magnetic bearing system, IEEE Trans. Control Syst. Technol. 19 (3) (2011) 636–643.

[61] K.M. Rahman, S. Hiti, Identification of machine parameters of a synchronous motor, IEEE Trans. Ind. Appl. 41 (2) (2005) 557–565.

[62] J. Pyrhönen, V. Hrabovcová, R. S. Semken, Electrical Machine Drives Control: An Introduction, Wiley, New York, USA, 2016.

[63] S. P. Bhat, D. S. Bernstein, Finite-time stability of continuous autonomous systems, SIAM J. Control Optim. 38 (3) (2000) 751-766.

[64] Y. B. Shtessel, I. A. Shkolnikov, A. Levant, Smooth second-order sliding modes: missile guidance application, Automatica 43 (8) (2007) 1470-1476.

[65] J.J.E Slotine, W. Li, Applied Nonlinear Control, Prentice Hall, Englewood Cliffs, USA, 1991.

[66] A. Gebregergis, P. Pillay, Implementation of fuel cell emulation on DSP and dSPACE controllers in the design of power electronic converters, IEEE Trans. Ind. Appl. 46 (1) (2010) 285–294.

[67] L. Zhang, H. Obeid, S. Laghrouche, M. Cirrincione, Second order sliding mode observer of linear induction motor, IET Electr. Power Appl. 13 (1) (2019) 38–47.

[68] X. Shen, J. Liu, W. Luo, J. I. Leon, S. Vazquez, A. Marquez, L.G. Franquelo, High-performance second-order sliding mode control for NPC converters, IEEE Trans. Ind. Inform. 16 (8) (2020) 5345–5356.

[69] Y. Huangfu, L. Guo, R. Ma, F. Gao, An advanced robust noise suppression control of bidirectional DC-DC converter for fuel cell electric vehicle, IEEE Trans. Transp. Electrification 5 (4) (2019) 1268–1278.